## Title

Sequential coupling of phase-field and vertex dynamics models for grain growth simulations



## Author

Ayyalasomayajula, Sai Deepak Kumar

## Publication Date

2024

Peer reviewed|Thesis/dissertation

UNIVERSITY OF CALIFORNIA
Los Angeles

# Sequential coupling of phase-field and vertex dynamics models for grain growth simulations

A thesis submitted in partial satisfaction
of the requirements for the degree
Master of Science in Materials Science and Engineering

by

Sai Deepak Kumar Ayyalasomayajula

2024

ABSTRACT OF THE THESIS

Sequential coupling of phase-field and vertex dynamics models for grain growth simulations

by

Sai Deepak Kumar Ayyalasomayajula
Master of Science in Materials Science and Engineering
University of California, Los Angeles, 2024
Professor Jaime Marian, Chair

Grain growth plays a pivotal role in determining the macroscopic properties of several polycrystalline materials. It is predominantly controlled by grain boundary and triple junction mobility, and several atomistic and mesoscale models have been developed to study this phenomenon. In particular, multi-order parameter phase-field and vertex dynamics models have been extensively used to understand the grain evolution dynamics and the effect of triple junction drag on the growth kinetics. In the current work, we present a novel sequentially-coupled phase-field and vertex dynamics model for both isotropic and anisotropic grain growth simulations. The proposed approach, which uses a backpropagation neural network, image processing and mathematical techniques for accurate grain boundary curvature detection, takes the advantages of both the models and provides an efficient way to switch from phase-field to vertex dynamics model depending on the growth controlling mechanism. Our results suggest that phase-field generated microstructures can replace Voronoi tessellation as the input to vertex dynamics, with a reduction in computational expenses and the ability to simulate more realistic and complex microstructures.

The thesis of Sai Deepak Kumar Ayyalasomayajula is approved.

Aaswath Pattabhi Raman

Amartya Sankar Banerjee

Jaime Marian, Committee Chair

University of California, Los Angeles

2024

*Dedicated to my parents, my brother, and my younger self, who decided to push through the hardships and chase his dreams . . .*

# Table of Contents

# List of Figures

# List of Tables

# Acknowledgements

I would like to express my sincere gratitude to my advisor, Professor Jaime Marian. Without his unwavering support throughout my time at UCLA, this work would not have been possible. I would also like to thank him for giving me the creative freedom to pursue independent research and providing me with invaluable career advice.

Furthermore, I would like to acknowledge my parents, my brother and my dear friend Anand Johnson for their unconditional love, guidance and encouragement.

# VITA

| | |
|---|---|
| 2016 – 2020 | B.Tech. in Metallurgical and Materials Engineering, National Institute of Technology (NIT), Warangal, India. |
| 2022 – Present | M.S. in Materials Science and Engineering, University of California, Los Angeles (UCLA). |

## Publications


[1] Sai Deepak Kumar, A., Pattanayak, D.K., Fayaz Anwar, M. et al. The Effect of Porosity, Oxygen and Phase Morphology on the Mechanical Properties of Selective Laser Melted Ti-6Al-4V with Respect to Annealing Temperature. Trans Indian Inst Met 76, 1789–1798 (2023).

[2] Kumar, A. Sai Deepak, Mohammad Fayaz Anwar, E. Vara Prasad, P. Bharath Sreevatsava, and C. Vanitha. "Effect of temperature and load during hot impression creep of Cu-Zn-Al alloy." Materials Today: Proceedings 39 (2021): 1296-1302.

[3] Kumar, A. Sai Deepak, M. S. Bhaskar, Suman Sarkar, and T. A. Abinandanan. "Phase Field Modelling of Precipitate Coarsening in Binary Alloys with Respect to Atomic Mobility of Solute in the Precipitate Phase." Transactions of the Indian Institute of Metals 73, no. 6 (2020): 1469-1474.

[4] Sreevatsava, P. Bharath, E. Vara Prasad, A. Sai Deepak Kumar, Mohammad Fayaz Anwar, Vadapally Rama Rao, and Vanitha Chilamban. "Effects of temperature and load during hot impression behavior of Cr-Ni stainless steel." Metallurgical and Materials Engineering 27, no. 4 (2021): 531-539.

# CHAPTER 1

# Introduction

Grain growth in polycrystalline materials is one of the most important phenomena that increases their grain size and has a profound impact on their thermal [1], electrical [2] and mechanical properties [3, 4, 5]. It is commonly observed in materials that undergo heat treatment, and understanding the thermodynamics and kinetics of the grain evolution process is paramount to designing materials for several structural and automotive applications. The fundamental mechanisms of grain growth have been well-researched. Burke and Turnbull [6] proposed that the driving force was the reduction in surface energy of grains, which was responsible for relaxation of grain boundaries towards their respective centers of curvature. Cole et al. [7] was the first to develop the square law $D^2 - {D_0}^2 = Kte^{\frac{-H}{kT}}$ for isothermal grain growth in steels, where "K" is a constant proportional to specific surface energy and atomic volume. However, the effect of grain size and shape distribution was not statistically considered in their approach. Feltham [8] developed a more comprehensive theory for grain growth in metals taking into account surface-tension affected curvature of grain boundaries, and proposed that grain size follows a log-normal distribution in addition to satisfying the square law $D^2 - {D_0}^2 = (\frac{\lambda V a \sigma}{b})te^{\frac{-H}{kT}}$, $\lambda$ being a constant of order 1 and $D, D_0$ are instantaneous and initial mean grain sizes.

Hillert [9] provided an exhaustive analysis of grain growth analogous to the precipitate coarsening theory by Lifshitz et al., [10]. He postulated that the driving force for grain growth is based on the capillary action, and that growth rate is only contingent upon the grain size of the material, although experiments carried out later [11] were in disagreement with this theory. Louat [12] implemented a stochastic method by considering the movement of grain boundaries and assumed no direct relationship between growth rate and grain size, in

that, grain size is only a function of boundary length. The combinations of the two theories, despite their individual limitations, have been developed and regarded as benchmark mean field theories to study grain growth today.

Despite varied assumptions, all the aforementioned theories result in the same conclusion i.e., $\overline{R}^2 \propto t$, where $\overline{R}$ is the mean grain size, but do not take into account the topological requirements during the grain growth process [13]. C.S. Smith [14] emphasized that topology is a marriage between space-filling and the geometrical need to achieve tension equilibrium at the surface. He developed a cellular model of the grain structure, in which vertices (V) are connected by edges (E), surrounded by faces (F) and satisfy the equation $F - E + V = 1$ in 2D. This representation led to the criterion that grains with less than 6 sides shrink and more than 6 sides grow, while adjusting their curvature to maintain a 120° angle at the vertices. Von Neumann [15] argued that it was surface tension and not geometrical necessity that acts as an impetus for grain growth. Mullins [16] arrived at the same conclusion, considering the area of a single grain, A, and formulated the expression, famously known as **von Neumann-Mullins topological law:**

$$\dot{A} = \frac{k\pi}{3}(s - 6). \tag{1.1}$$

where $s$ is the number of sides of grain and $\dot{A}$ is the rate of area change.

However, Rivier [17] asserted that surface tension does not affect the rate of change of grain area. He proved that the process is purely driven by the tendency for space-filling and that the size distribution statistics remain invariant despite topological transformations affecting the shape of grain during evolution. Kurtz and Carpay [18, 19], further extended the initial works of Feltham [8] by categorizing each grain into a topological class and elucidated that log-normal distribution is one of the essential characteristics of grain growth in a material.

Grain growth can be broadly divided into two types: (1) Normal (NGG) and (2) Abnormal grain growth (AGG). The principles of Hillert [9] and von Neumann-Mullins [15] are applicable to NGG and can be extended to abnormal condition. While NGG assumes

that grain boundaries migrate at a constant rate i.e., the grain boundary mobility is constant and the driving force is reduction in grain boundary energy , AGG is affected by local variations or anisotropy in energy and mobility due to the presence of defects and secondary phase [20, 21, 22]. Moreover, the distribution of grain size is remarkably different, with NGG displaying an invariant and more uniform nature as compared to abnormal growth [23, 24, 25]. Although there are many theories on both NGG and AGG, a general theory has been developed by Hu et al. [26] by implementing a coupling factor into their model. They predicted that grain growth is predominantly controlled by the combination of grain size, grain boundary free energy and local size distribution. But another pivotal aspect that decides growth rate is triple junctions (TJ) at the grain boundary. These are regions where three grain boundaries from different grains intersect each other. Czubayko et al., [27] experimentally studied the TJ effect and observed that a low TJ mobility induced drag on the grain boundaries, thereby resulting in sluggish growth kinetics. However, when the TJ mobility is high, the growth was primarily defined by grain boundary motion. Atomistically, grain growth can be manifested as (1) the diffusion of atoms from the shrinking to growing grain and (2) the subsequent incorporation of these atoms into the larger grain [28] and the slowest step would determine the rate of grain growth.

The current comprehension of various mechanisms in grain growth can be attributed to the tailored experiments and the rise of computational models in the past few years. Especially computer simulations have played a major role in supporting the mathematical theories, and validating the experimental results [29, 30, 31, 32, 33, 34, 35], expanding our perspective. There are many grain growth models, but they can be broadly classified as: (1) Stochastic and (2) Deterministic. Stochastic techniques are based on the understanding of electron spins in statistical physics and are known for their simplicity and ease of computation in both 2D and 3D. Some examples include Potts model [36, 37, 38] and kinetic Monte Carlo (kMC) model [39, 40]. Deterministic models, on the other hand, require that the motion of grain boundaries be defined and assume driving forces to be directly proportional to the boundary velocity. Phase-field (PFM) [41, 42, 43] and vertex models [44, 45] fall under this

category. Unlike stochastic methods, these models can explain the kinetics of all the grain boundaries in a material, making the study of misorientation and anisotropic properties much simpler.

Several attempts were made to couple the deterministic - stochastic and stochastic - stochastic approaches, and leverage their individual advantages for a deeper understanding of the grain evolution dynamics [46, 47, 48, 49]. Tran eta al., [50] integrated Potts, kMC and PFM and deduced that 2D grain growth could be akin to geometric Brownian motion. Such important analogies, along with various perspectives, could be developed by hybrid models. However, this idea has been largely unexplored between two deterministic models.

In the present work, we combine phase-field and vertex dynamics (VD) [51] methods through back-propagation neural network, image processing and mathematical techniques. The misorientation, grain boundary curvature, grain boundary energy and mobility are directly transferred from PFM to VD, without the need for a Voronoi tessellation in the latter. Although the two models largely vary in their formulation and tackle different features of a microstructure, their effective combination could significantly reduce the computational times required for grain growth simulations, since VD is **two orders of magnitude** faster than PFM [52]. These models, along with the switching from grain boundary migration controlled kinetics in PFM to TJ controlled in VD during coupling are explained in detail in Chapter 2.

# CHAPTER 2

# Theory of phase-field and vertex dynamics models

## 2.1 Phase-field model

Grain growth, or any microstructural evolution, entails a reduction in free energy of the material system. This free energy can be of any form; bulk, interfacial, magnetic and elastic strain to name a few. Several numerical techniques have been developed to model such complex transformations, with an assumption that the boundaries between different compositional domains in the microstructure could be simplified as sharp interfaces [53, 54, 55]. Conventional statistical models track grain boundary interfaces explicitly to calculate the velocity with respect to boundary mobility, which becomes exceedingly difficult as one goes to three dimensions. This problem can be addressed by phase-field methods.

Phase-field models offer a continuum approach with finite interface thickness (diffuse interface) and a sharp interface limit [56]. Two major equations describe the microstructural evolution: (1) Cahn-Hilliard (C-H) [57] and (2) Allen-Cahn (A-C) [58]. These models implicitly track the interfaces with the help of phase-field and are a go-to choice for the simulation of solidification of molten metal or alloy pools. Another section of applications of these models involves assigning order parameters to various microscopic properties of interest, such as misorientation, composition etc., and performing temporal evolution of these parameters with C-H or A-C equations.

The order parameters are further subdivided into two types based on the local property conservation as conserved (eg., composition) and non-conserved (eg., grain orientation). A general formulation used in PFM with these parameters is given below.

### 2.1.1 Total Free Energy

The total free energy described by conserved $(c_1, c_2, ....)$ and non-conserved $(\eta_1, \eta_2, ....)$ order parameters is a Ginzburg-Landau free energy functional 'F', given by

$$F = \int [f(c_1, c_2, \ldots, c_n, \eta_1, \eta_2, \ldots, \eta_p) + \sum_{i=1}^{n} \alpha_i (\nabla c_i)^2 + \sum_{i=1}^{3} \sum_{j=1}^{3} \sum_{k=1}^{p} \beta_{ij} \nabla \eta_{ik} \nabla \eta_{jk}] d^3r + \iint G(\mathbf{r} - \mathbf{r}') d^3r d^3r'. \quad (2.1)$$

where 'f' is the local free energy density, $\alpha_i$ and $\beta_{ij}$ are gradient energy coefficients. The first integral is the local free energy arising from short-range chemical interactions while the second is from long-range.

### 2.1.2 Local Free Energy

Several phase-field models use a double-well function for local free energy. This is because these functions are consistent with the Landau theory for phase transitions, have two minima, and represent two bulk phases in the system, solid-liquid or solid-solid. Between the two minima, the order parameter varies, indicating a diffuse interface. Moreover, the double-well function has a relatively simple form that reduces the computational expenses. An example of such a function used in the phase-field grain growth simulations with infinite number of minima is given in equation 2.2 and shown in Fig. 2.1.

$$f(\phi_1, \phi_2, ...) = 4\Delta f \left( -\frac{1}{2} \sum_i \phi_i^2 + \frac{1}{4} \sum_i \phi_i^4 \right) + \alpha \sum_i \sum_{j>i} \phi_i^2 \phi_j^2. \quad (2.2)$$

$\alpha$ is a positive constant and $\Delta f$ is energy barrier between the minima. All the infinite minima are located at (1,0,0,...), (-1,0,0,...), (0,1,0,...), which are essentially order parameters $(\phi)$ assigned to different grain orientations.

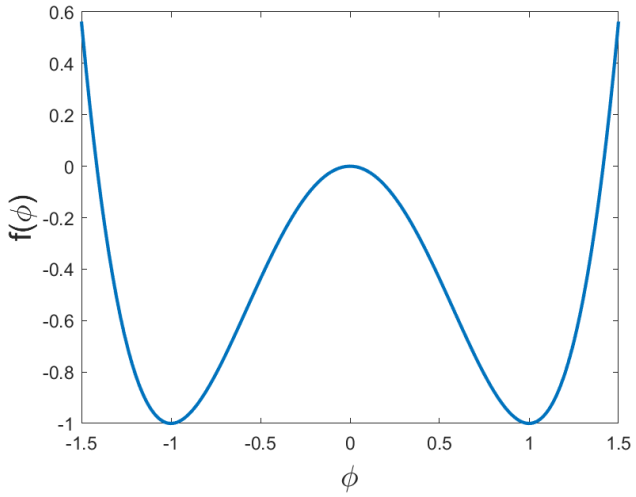


Fig. 2.1: Double-well local free energy function.

### 2.1.3 Gradient Energy

The excess free energy due to inhomogeneties corresponds to the interfacial energy. The total free energy can be simplified in terms of bulk and interfacial free energies as

$$F = F_{\text{bulk}} + F_{\text{int}} = \int_V \left[ f(\phi) + \frac{1}{2}\kappa(\nabla\phi)^2 \right] dV. \tag{2.3}$$

$\kappa$ is the gradient energy coefficient. If $\phi$ is a long-range order parameter, then interfacial energy per unit area ($\gamma$) can be expressed as

$$\gamma = \frac{4\sqrt{2}}{3}\sqrt{\kappa \Delta f}. \tag{2.4}$$

### 2.1.4 Temporal evolution of order parameters

Cahn-Hilliard (equation 2.5) and Allen-Cahn (equation 2.6) equations are widely used for the evolution of conserved $(c_1, c_2, ...)$ and non-conserved $(\eta_1, \eta_2, ...)$ order parameters respectively. Then, finite difference or spectral methods are implemented with boundary conditions in a spacial grid to obtain the solutions, and thus, the kinetics of the process.

$$\frac{\partial c_i(\mathbf{r},t)}{\partial t} = \nabla M_{ij} \nabla \frac{\delta F}{\delta c_j(\mathbf{r},t)}, \tag{2.5}$$

$$\frac{\partial \eta_p(\mathbf{r},t)}{\partial t} = -L_{pq} \frac{\delta F}{\delta \eta_q(\mathbf{r},t)}. \tag{2.6}$$

$M_{ij}$, $L_{pq}$ are order parameter mobilities that can be correlated to interfacial mobility. All the equations are adopted form [59].

In the present work, we place emphasis on the grain growth kinetics with A-C equation, which is briefly elucidated in the methodology section.

## 2.2 Vertex Dynamics model

### 2.2.1 VD Formulation

In contrast to PFM, VD model treats the grain boundary motion explicitly with well-defined equations. It was first proposed by Weygand [45] as a modified form of vertex model developed by Kawasaki et al., [60, 61]. The grain boundaries are, in general, defined by simple line segments connected at triple junctions, which are termed as "real vertices." Voronoi tessellation is the most commonly used initial microstructure due to its simplicity and the nature of the VD model. Discretization points or "virtual vertices" are introduced between two real vertices to take into account the curvature effect. The microstructure is represented by positions (r) of these vertices and the corresponding velocities (v). An energy or potential term $V(r)$, usually interfacial or surface energy, describes the system along with a drag term, $R(r,v)$, which opposes the motion of the grain boundaries during evolution. The equations involved in the 2D VD method are:

$$V\{\vec{r}\} = \int_{\text{GBs}} \gamma(a)\, da, \tag{2.7}$$

$$R\{\{\vec{r}\},\{\vec{v}\}\} = \frac{1}{2} \int_{\text{GBs}} \frac{v(a)^2}{m_{\text{GB}}(a)}\, da. \tag{2.8}$$

Here, 'a' is a curvilinear position (coordinate) along the grain boundary GB, '$\gamma$' is the surface energy at position 'a', and '$m_{GB}$' is the GB mobility at position 'a'. For a given line segment $ij$ between positions $r_i, r_j$, the velocity $v_{ij}$ and normal to $r_{ij}$ are:

$$\vec{v_{ij}} = \xi\vec{v_i} + (1-\xi)\vec{v_j}, \tag{2.9}$$

$$\vec{n}_{ij} = \frac{1}{\|\vec{r}_{ij}\|}\begin{bmatrix} -y_{ij} \\ x_{ij} \end{bmatrix}. \tag{2.10}$$

$V(r)$ and $R(r,v)$ then become:

$$V(\{\vec{r}_n\}) = \frac{1}{2}\sum_{i=1}^{N}\sum_{j}^{i}\gamma_{ij}\|\vec{r}_{ij}\|, \tag{2.11}$$

$$R(\{\vec{r}_n\},\{\vec{v}_n\}) = \frac{1}{6}\sum_{i=1}^{N}\sum_{j}^{i}\frac{\|\vec{r}_{ij}\|}{m_{ij}}\left[(\vec{v}_i\cdot\vec{n}_{ij})^2 + (\vec{v}_j\cdot\vec{n}_{ji})^2 + (\vec{v}_i\cdot\vec{n}_{ij})(\vec{v}_j\cdot\vec{n}_{ji})\right]. \tag{2.12}$$

In equations 2.11 and 2.12 each vertex is associated only with its neighbors, which gives us a localized understanding of the microstructure around individual vertices. Lagrange equation is implemented to calculate the discrete sum of these equations over each line segment to obtain a relationship between local driving force and velocity.

$$\frac{\partial V(\{\vec{r}_n\})}{\partial\vec{r}_i} + \frac{\partial R(\{\vec{r}_n\},\{\vec{v}_n\})}{\partial\vec{v}_i} = 0, \quad i,n = 1,\ldots,N. \tag{2.13}$$

The velocity of each vertex is calculated by coupling the equations 2.11 - 2.13:

$$D_i\vec{v}_i = \vec{f}_i - \frac{1}{2}\sum_{j}^{i}D_{ij}\vec{v}_j, \quad i = 1,\ldots,N. \tag{2.14}$$

where

$$D_{ij} = \frac{1}{3m_{ij}\|\vec{r}_{ij}\|}\begin{bmatrix} y_{ij}^2 & -x_{ij}y_{ij} \\ -x_{ij}y_{ij} & x_{ij}^2 \end{bmatrix}, \tag{2.15}$$

$$D_i = \sum_{j}^{i}D_{ij}, \tag{2.16}$$

$$\vec{f_i} = -\frac{\partial V}{\partial \vec{r_i}} = -\sum_{j}^{i} \gamma_{ij} \frac{\vec{r}_{ij}}{\|\vec{r}_{ij}\|}. \tag{2.17}$$

The motion of both real and virtual vertices is described by equation 2.14. A virtual vertex moves only when the two segments passing through it form an angle greater than 1°. The time step is incorporated into the equation as:

$$D_i(\{\vec{r}_{ij}(t)\})\vec{v}_i(t) = \vec{f_i}(\{\vec{r}_{ij}(t)\}) - \frac{1}{2}\sum_{j}^{i} D_{ij}(\{\vec{r}_{ij}(t)\})\vec{v}_j(t - dt), \tag{2.18}$$

$$\vec{r}_n(t + dt) = \vec{r}_n(t) + \vec{v}_n(t)\, dt. \tag{2.19}$$

All the equations are adopted from [51, 62].

### 2.2.2 Topological Transformations

Topological changes occur during grain growth due to grain boundary migration, which causes the boundary to move towards its center of curvature. TJ motion is also a contributing factor for the annihilation of smaller grains and the restructuring of larger grains. The conventional von Neumann-Mullins law does not consider the effect of TJs. A modified version of the law [63], with TJ effect represented by an angle $\theta$ is given by:

$$\dot{S} = -\frac{A_b}{1 + \frac{1}{\Lambda}} \left[2\pi - n(\pi - 2\theta)\right], \tag{2.20}$$

$$A_b = m_b \gamma_b, \tag{2.21}$$

$$\Lambda = \frac{2\theta}{2\cos\theta - 1}, \quad n < 6, \tag{2.22}$$

$$\Lambda = -\frac{\ln \sin\theta}{1 - 2\cos\theta}, \quad n > 6. \tag{2.23}$$

$A_b$ is the reduced mobility, $m_b$ is the GB mobility, $\gamma_b$ is the surface energy at the GB, $\theta$ is the angle at TJ, $n$ is the number of sides of grain and $\Lambda$ is the dimensionless criterion. According to this equation, the rate of shrinkage of smaller grains is reduced due to the finite mobility of TJs and grains with $n > 6$ are subjected to drag, decreasing their growth rate.

There are three topological changes that occur during VD; T1, T2 and T3. T1 involves connecting two TJs close to each other ($< l_{threshold}$) to form a quadruple junction (QJ) [64], which then dissociates due to its unstability into configuration E1 if its energy is less than the original configuration. T2 removes grains with less than 4 sides below an area threshold ($< A_{threshold}$). Small grains with two TJs are annihilated in T3. These processes are illustrated in Fig. 2.2.

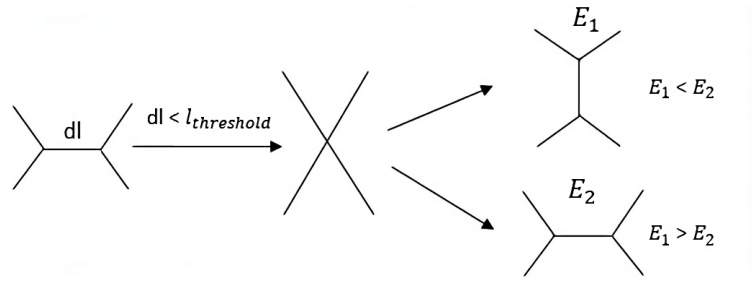


(a) T1

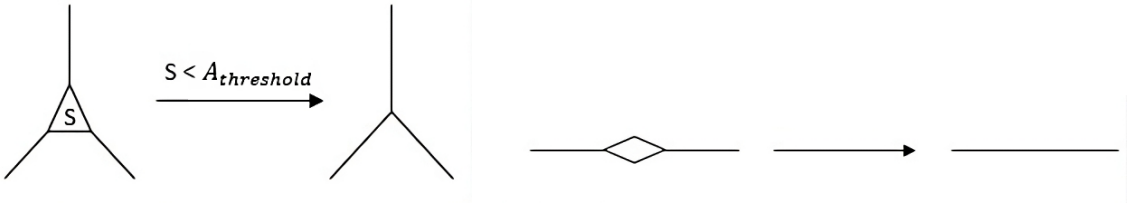


(b) T2

(c) T3

Fig. 2.2: Topological transformations.

## 2.3 Advantages of coupling Phase-Field and Vertex Dynamics

In the early stages, grain growth is driven by grain boundary energy reduction. Grain boundaries with higher curvature have a higher driving force for migration since the pressure exerted on grain boundary is proportional to its curvature according to Young-Laplace equation, and they gradually flatten out . Larger grains grow at the expense of smaller grains in a self-similar manner, with uniform grain size distribution. However, as growth progresses, TJ mobility starts dominating [65], and equilibrium is attained when the forces at each junction by the connected grain boundaries are balanced (Herring condition).

PFM efficiently captures the curvature effects but VD facilitates a better handling of triple and quadruple junctions overall. Despite previous attempts to study topological transformations in PFM [66, 67, 68] , coupling phase-field and vertex dynamics would prove to be effective in cases where one of the controlling mechanisms is negligible as grain evolution occurs, and helps reduce the computational time. Furthermore, Voronoi tessellation can be superseded with complex and more realistic microstructures imported from PFM as the input to VD.

# CHAPTER 3

# Methodology

## 3.1 PFM for isotropic and anisotropic grain growth

All the phase-field codes were developed using MATLAB and simulated in a multi-threading environment over 8 cores. A multi-order parameter phase-field model was partially adopted from Moleans et al., [69]. We define a single phase material with 15 different non-conserved order parameters $(\eta_1(r,t), \eta_2(r,t), ...\eta_{15}(r,t)) = [(1,0,0...0), (0,1,0,...0)..., (0,0,0,...1)]$ representing random grain orientations on a mesh grid. Each order parameter represents multiple grains with same orientation. Anisotropy was introduced by making gradient energy coefficient ($\kappa$) a function of misorientation ($\theta$). The order parameter mobility ($L$) was considered to be constant. Here, we discuss the formulation for anisotropic grain growth, which is valid for isotropic case as well when '$\kappa$' is made constant. The temporal evolution of order parameters is given by the time-dependent Ginzburg-Landau equation as:

$$\frac{\partial \eta_i}{\partial t} = -L\frac{\delta F}{\delta \eta_i}. \tag{3.1}$$

where

$$F = \int_V \left[ f(\eta_1, \eta_2, \ldots) + \sum_{i=1}^{N} \frac{\kappa_i(\theta)}{2} |\nabla \eta_i|^2 \right] dV, \qquad \theta \in (0, 30) \tag{3.2}$$

$$f(\eta_1, \eta_2, \ldots) = \sum_{i=1}^{N} \left( -\frac{A}{2}\eta_i^2 + \frac{B}{4}\eta_i^4 \right) + \sum_{i=1}^{N}\sum_{j>i}^{N} C_{i,j}(\theta)\eta_i^2\eta_j^2 + \frac{1}{4}. \tag{3.3}$$

A and B are constants. C is a phenomenological parameter and is a function of misorientation. For two grains $1, 2$ with orientations $\theta_1, \theta_2$ (see Fig. 3.1), misorientation is

$$\theta_{1,2} = |\theta_1 - \theta_2| \tag{3.4}$$

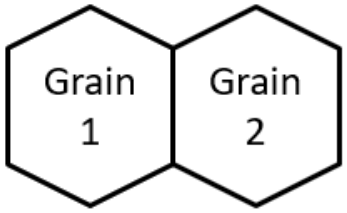


Fig. 3.1: Grains with orientation $\theta_1$, $\theta_2$.

However, in our simulation, misorientation was first calculated between each order parameter with unique orientation. Then, the grain boundary energy was calculated by using the Read-Shockley expression,

$$\gamma_{\mathrm{GB}}(\theta_{1,2}) = \begin{cases} \gamma_m \frac{\theta_{1,2}}{\theta_m}\left(1 - \ln\left(\frac{\theta_{1,2}}{\theta_m}\right)\right) & \text{if } \theta_{1,2} < \theta_{\max}, \\ \gamma_m & \text{if } \theta_{1,2} \geq \theta_{\max}. \end{cases} \tag{3.5}$$

All the grain boundaries with misorientation less than $\theta_{max}$ are low-angle grain boundaries (LAGBs). For the high-angle grain boundaries (HAGBs), the energy was assumed to be constant ($\gamma_m$). For simplicity, the effect of GB inclination on the energy was not taken into account. $\kappa(\theta)$ and C($\theta$)can be expressed as a function of $\gamma(\theta)$:

$$\kappa(\theta_{1,2}) = \kappa_m \frac{\gamma(\theta_{1,2})}{\gamma_m}, \tag{3.6}$$

$$C(\theta_{1,2}) = \frac{1}{2}\frac{\left(4\kappa(\theta_{1,2})m + 9\gamma(\theta_{1,2})\right)^2}{\left(4\kappa(\theta_{1,2})m - 9\gamma(\theta_{1,2})\right)^2}. \tag{3.7}$$

The parameter 'm' is a normalization constant. We assume that the grain boundary width is constant throughout. With this established, the evolution equation 3.1 was discretized with first-order semi-implicit Fourier spectral scheme [70], since this method offers stability with large time steps (n). The parameters used in simulation are tabulated in table 3.1.

$$\frac{\partial \eta_i}{\partial t} = -L\frac{\delta f}{\delta \eta_i} + L\kappa\nabla^2\eta_i, \quad i = 1, 2, \ldots, N. \tag{3.8}$$

$$\frac{\partial \eta_i}{\partial t} = \frac{\eta_i^{n+1} - \eta_i^n}{\Delta t} = -L\left(-A\eta_i^n + B(\eta_i^n)^3 + 2C(\theta)_{ij}\eta_i^n \sum_{i\neq j}^{N}(\eta_j^n)^2 - \kappa(\theta)\nabla^2\eta_i^{n+1}\right), \tag{3.9}$$

In Fourier space, $\eta_i$ and $f$ are $\tilde{\eta_i}$ and $\tilde{f}$ related with a wave vector, k = $(k_1, k_2)$.

$$\frac{\partial \tilde{\eta_i}}{\partial t} = -L\left(\frac{\delta \tilde{f}}{\delta \eta_i}\right) - k^2 L\kappa(\theta)\tilde{\eta_i}, \tag{3.10}$$

$$\frac{\tilde{\eta_i}^{n+1} - \tilde{\eta_i}^{n}}{\Delta t} = -L\left(\frac{\delta \tilde{f}}{\delta \eta_i}\right)^n - k^2 L\kappa(\theta)\tilde{\eta_i}^{n+1}, \tag{3.11}$$

$$\tilde{\eta_i}^{n+1} = \frac{\tilde{\eta_i}^{n} - \Delta t L\left(\frac{\delta \tilde{f}}{\delta \eta_i}\right)^n}{1 + \Delta t L\kappa(\theta)k^2}. \tag{3.12}$$

Table 3.1: Parameters used in PFM simulation of isotropic and anisotropic grain growth.

| **Dimensionless Parameter** | **Isotropic grain growth** | **Anisotropic grain growth** |
|---|---|---|
| System Size | 512 x 512 | 512 x 512 |
| $dx, dy$ | 1 | 1 |
| $dt$ | 0.1 | 0.1 |
| Total time, $t$ | 100 | 100 |
| A | 1 | 1 |
| B | 1 | 1 |
| C | 1 | 1 |
| L | 1 | 1 |
| $\kappa_m$ | 1 | 1 |
| Energy parameter, $\epsilon_0$ | 0.05 | 0.05 |
| $\gamma_m = \frac{1}{1+\epsilon_0}$ | 0.952 | 0.952 |
| $n$ (order parameters) | 15 | 15 |
| m | - | 2.5 |
| $\theta_{\max}$ | - | 15° |

Equation 3.12 was solved for all the grid points on the mesh grid. Periodic boundary conditions were implemented. From the final PFM microstructure, grains belonging to the same orientation ($\eta_i$) were identified and labeled. The misorientation between order parameters was assigned to their constituent grains using these labels.

## 3.2 Transformation of PFM microstructure into vertex representation for VD

### 3.2.1 Conversion to binary image and detection of grain boundary edges with Backpropagation Neural Network

In order to couple PFM output to the VD model, we first converted the PFM microstructure into a binary image. This was done using image segmentation by Otsu's threshold selection method [71] with MATLAB image processing toolbox. It is a nonparametric and unsupervised technique that takes an image with different gray levels and utilizes an optimum threshold value to maximize the gray-class variance. However, detection of small morphological features was affected because of their relatively low intensity peaks and the method's inherent assumption of bimodal distribution of pixel intensities. Although local thresholding was adopted to alleviate this problem, it was sensitive to parameters such as window and filter size and produced inconsistent results for different microstructures.

Therefore, we employed edge-detection method using Levenberg-Marquardt Backpropagation neural network (BP NN) proposed by Mehrara et al., [72], which takes the binary input and removes the pseudo noise around the grain edges to accurately detect the pixels on grains and grain boundaries. This could help in customized noise removal in less than a few seconds by training the NN with the desired input and output patterns. First, the binary image was taken and the pixels (black - 0, white -1) were divided into 2x2 windows, which serve as input to NN. The network structure contains 4 input and 4 output neurons, with 16 hidden neurons as shown in Fig. 3.2 and table 3.2 (adopted from [72])). Sigmoid function was used as an activation function to get only '1's and '0's as the final network output. The NN was trained for 1000 epoch with 16 patterns as input, a backpropagation learning rate of 0.01 and momentum 0.9. This value of momentum is commonly used to prevent the process from converging at a local minima. A brief algorithm for the NN is shown below.

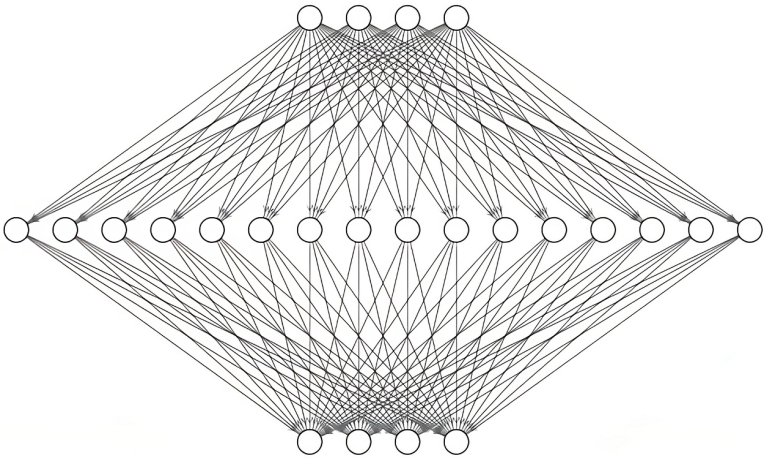

Fig. 3.2: Neural network showing 4 input, 16 hidden and 4 output neurons.

Table 3.2: The input and output for pre-trained patterns.©2009 IEEE.

| **Pattern no.** | **Input pattern** | **Detected as** | **Output pattern** |
|---|---|---|---|
| 1 | 0 0 0 0 | None edge | 1 1 1 1 |
| 2 | 0 0 0 1 | Corner edge | 0 0 0 1 |
| 3 | 0 0 1 0 | Corner edge | 0 0 1 0 |
| 4 | 0 0 1 1 | Horizontal edge | 0 0 1 1 |
| 5 | 0 1 0 0 | Corner edge | 0 1 0 0 |
| 6 | 0 1 0 1 | Parallel edge | 0 1 0 1 |
| 7 | 0 1 1 0 | Diagonal edge | 0 1 1 0 |
| 8 | 0 1 1 1 | Pseudo noise | 1 1 1 1 |
| 9 | 1 0 0 0 | Corner edge | 1 0 0 0 |
| 10 | 1 0 0 1 | Diagonal edge | 1 0 0 1 |
| 11 | 1 0 1 0 | Parallel edge | 1 0 1 0 |
| 12 | 1 0 1 1 | Pseudo noise | 1 1 1 1 |
| 13 | 1 1 0 0 | Horizontal edge | 1 1 0 0 |
| 14 | 1 1 0 1 | Pseudo noise | 1 1 1 1 |
| 15 | 1 1 1 0 | Pseudo noise | 1 1 1 1 |
| 16 | 1 1 1 1 | None edge | 1 1 1 1 |

**Algorithm 1 :** BP NN for edge detection and noise removal in binary image.

**Initialize:** Input pattern $s$, Output pattern $t$, number of patterns $Pattern$, epochs $Epoch$, input neurons $N_1$, hidden neurons $N_2$, output neurons $N_3$, learning rate $\alpha$, weights $V, W$, biases $V_0, W_0$, velocity terms $vel_V, vel_W, vel_{V_0}, vel_{W_0} = 0$

**for** $iter = 1$ to $Epoch$ **do**

  **for** $p = 1$ to $Pattern$ **do**

    Set $X = s(p, :)$

    **Forward Propagation:**

    **for** $j = 1$ to $N_2$ **do**

      $Zin_j = V_0 + \sum_{i=1}^{N_1} X_i \cdot V_{ij}$ {Add bias to N2 layer output}

      $Z_j = \text{Sigmoid}(Zin_j)$ {Activation function}

    **end for**

    **for** $k = 1$ to $N_3$ **do**

      $Yin_k = W_0 + \sum_{j=1}^{N_2} Z_j \cdot W_{jk}$ {Add bias to N3 layer output}

      Set $Y_k = Yin_k$

    **end for**

    **Backpropagation:**

    **for** $k = 1$ to $N_3$ **do**

      $\delta_k = (t_{pk} - Y_k) \cdot \text{Sigmoid}'(Yin_k)$ {Output layer error}

      $\Delta W_{jk} = \alpha \cdot \delta_k \cdot Z_j$ {Update weights}

      $\Delta W_0 = \alpha \cdot \delta_k$ {Update biases}

      Update velocity and weights using momentum for $W$ and $W_0$

    **end for**

    **for** $j = 1$ to $N_2$ **do**

      $\delta_j = \left(\sum_{k=1}^{N_3} \delta_k \cdot W_{jk}\right) \cdot \text{Sigmoid}'(Zin_j)$ {Hidden layer error}

      $\Delta V_{ij} = \alpha \cdot \delta_j \cdot X_i$ {Update weights}

      $\Delta V_0 = \alpha \cdot \delta_j$ {Update biases}

      Update velocity and weights using momentum for $V$ and $V_0$

    **end for**

  **end for**

**end for**

### 3.2.2 Pixel thinning of grain boundaries using Zhang-Suen thinning algorithm

To convert the grain boundaries with finite thickness in PFM microstructure to thin lines consisting of single pixels across the boundary length, the resulting binary image from the previous step was subjected to Zhang-Suen pixel-by-pixel thinning [73]. It is an iterative procedure where in each iteration, the algorithm checks the 8 neighborhood of a pixel and removes the it if the pixel contains exactly one transition from white (1) to black (0) pixel and has at least 1 black pixel as its neighbor, but not more than 6. This is repeated for two iterations with different sets of pixel neighbors to uniformly thin the grain boundaries. Moreover, we modified the algorithm to scan in a 4-neighborhood at the edges to include the pixels on the perimeter. The algorithm is provided in appendix A.

### 3.2.3 Establishing pixel connectivity and grain boundary shape construction

Individual grain and grain boundary (pixel positions) regions were identified from the pixelated image and the grain labels from PFM were precisely reassigned to the GB thinned microstructure. Depending on the pixel neighborhood at the intersection points of grain boundaries, the junctions were categorized into triple (3 grains in the neighborhood), quadruple junctions (4 grains in the neighborhood)and higher order junctions (>4 grains in the neighborhood). These junctions are the 'real vertices' in VD model. Once the grains attached to each vertex were identified, the inter-junction (node) connectivity was established by locating the junctions that belong to the same grain boundary. The pixels connecting any two junctions could be seen as 'virtual vertices', discretizing the grain boundary. Appendix B can be referred for a detailed algorithm on pixel connectivity.

The grain boundary curvature was constructed between each pair of junctions by fitting a circle along the virtual vertices using the algorithm developed by Taubin [74]. The technique calculates the average position of the virtual vertices first, adjusts the positions of all the other vertices relative to this center and calculates their distance. The distances and positions are then processed by a mathematical technique 'Singular Value Decomposition (SVD)',

which factorizes the virtual vertices matrix into three other matrices: two orthogonal and one diagonal matrix with singular values. Through these, geometric properties of the original matrix are predicted. In our case, we accurately determined the radius and center of the circular arc fitted along virtual vertices, and built a vertex representation of the original PFM microstructure using this radius. The algorithm for the same is given below.

**Algorithm 2 :** Grain boundary curvature construction from virtual vertices.

1: **Input:** `vertices` of size `[n,2]`

2: **Output:** Circle parameters `[a, b, R]` with center `[a,b]`, radius `R`

3: Compute the centroid $\mathbf{c}$

$$\mathbf{c} = \left( \frac{1}{n} \sum_{i=1}^{n} x_i, \frac{1}{n} \sum_{i=1}^{n} y_i \right)$$

4: Normalize coordinates: $X_i = x_i - c_x$, $Y_i = y_i - c_y$

5: Compute distances from centroid: $Z_i = X \odot X + Y \odot Y$

6: Compute mean of distances: $Z_{\text{mean}} = \frac{1}{n} \sum_{i=1}^{n} Z_i$

7: Normalize distances: $Z_{0i} = \frac{Z_i - Z_{\text{mean}}}{2\sqrt{Z_{\text{mean}}}}$

8: Construct matrix for SVD: $\mathbf{Z}_{\text{points}} = \begin{bmatrix} Z_{0i} & X_i & Y_i \end{bmatrix}$

9: Perform SVD on $\mathbf{Z}_{\text{points}}$: $\mathbf{U}, \mathbf{S}, \mathbf{V}^T = \text{SVD}(\mathbf{Z}_{\text{points}})$

10: Extract third column of $\mathbf{V}$ as vector $\mathbf{A}$

11: Adjust $A_1$: $A_1 = \frac{A_1}{2\sqrt{Z_{\text{mean}}}}$

12: Augment $\mathbf{A}$: $\mathbf{A} = \begin{bmatrix} A_1 \\ A_2 \\ A_3 \\ -Z_{\text{mean}} \cdot A_1 \end{bmatrix}$

13: Calculate circle center:

$$\begin{bmatrix} a \\ b \end{bmatrix} = -\frac{1}{A_1/2} \begin{bmatrix} A_2 \\ A_3 \end{bmatrix} + \mathbf{c}$$

14: Calculate radius:

$$R = \frac{\sqrt{A_2^2 + A_3^2 - 4 \cdot A_1 \cdot A_4}}{|A_1/2|}$$

## 3.3 Vertex Dynamics model with input from PFM

### 3.3.1 Equations of motion

VD was implemented on the vertex image obtained from the previous step. The constituent equations for velocities ($v_{TJ}$) and forces ($F_{GB}$) acting on the junctions in our model are:

$$v_{TJ} = M_{TJ} \sum_{i=1}^{k} F_{GB}^{i} \tag{3.13}$$

$$F_{GB}^{i} = \gamma_{GB}^{i} \vec{t^{i}} \tag{3.14}$$

$$F_{GB}^{i} = \sum_{i=1}^{k} \gamma_{GB}^{i} \vec{t^{i}} \frac{\vec{u^{i}}}{\|\vec{u^{i}}\|} \tag{3.15}$$

where $k$ is the number of grain boundaries attached to a junction i and $\vec{t^{i}}$ is a tangent at junction $i$ of the grain boundary (see Fig. 3.4). $\frac{\vec{u^{i}}}{\|\vec{u^{i}}\|}$ is the unit vector joining the junction to its adjacent boundary point and decides the direction of motion. It should be noted that the Herring condition is not artificially imposed here, but it naturally arises from the curvature induced forces that leads to the movement of vertices towards equilibrium shape. The dimensionless parameter, $\Lambda = \bar{D}\frac{M_{TJ}}{M_{GB}}$ was taken to be <1 with average grain size, $\bar{D}$, normalized to unity [75], so that the vertex motion is TJ controlled. Because of low $M_{TJ}$, the kinetics deviate significantly from that predicted by von Neumann-Mullins relationship [76]. $M_{GB}$ was considered to be the same as the order parameter mobility, L from PFM.

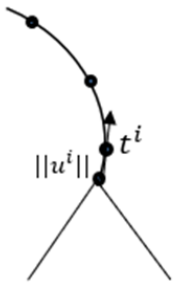


Fig. 3.3: Discretized grain boundary showing tangent, $\vec{t^{i}}$, to the grain boundary and unit normal, $\frac{\vec{u^{i}}}{\|\vec{u^{i}}\|}$, at the junction.

### 3.3.2 Grain Boundary energy

Grain boundary energy was calculated in a similar manner as in PFM using equation 3.5. For the initial microstructure of VD, the misorientation and grain boundary energy were directly imported from the final microstructure of the phase-field model based on the grain labels. This misorientation does not change with time since the deformation effects are ignored in our current model and hence, the grain boundary energy for a specific misorientation remains constant throughout the simulation (same as in PFM).

### 3.3.3 Read-Shockley and curvature force calculation

Read-Shockley energy for each GB was projected along $\frac{\vec{u^i}}{\|\vec{u^i}\|}$ to obtain the Read-Shockley force acting on the GB's associated junctions. This force was substituted in equation 3.13 to obtain the junction velocity. Curvature force was calculated using the method described in [75] and is discussed here for completeness. If $S1$ is a spherical surface having a surface tension $\gamma$ defined by normal $n$ and has lengths $b, h$ and $r$, as shown in Fig. 3.4, and $S2$ is an equivalent flat surface, then,

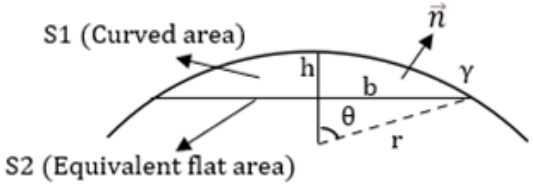


Fig. 3.4: Geometric model for curvature force calculation from a curved grain boundary.

$$A_{S1} = \pi(b^2 + h^2) \tag{3.16}$$

$$A_{S2} = \pi b^2 \tag{3.17}$$

The change in energy when curved surface transforms to a flat line segment is

$$\Delta E = \gamma(A_1 - A_2) = \gamma\pi h^2$$

$$F_\gamma = -\frac{d\Delta E}{dh} = -2\gamma\pi h$$

From the geometry, $r^2 = b^2 + (r-h)^2$. Assuming $h \ll r$:

$$h \approx \frac{b^2}{2r}$$

which gives:

$$F_\gamma = -\frac{\gamma \pi b^2}{r}$$

$F_\gamma$ is normalized by the grain boundary area $A_2$ to find the changes in force solely due to curvature. This results in:

$$f_\gamma = \frac{F_\gamma}{A_2} = -\frac{\gamma}{r}$$

The radius $r$ to calculate the curvature force was determined by the grain boundary construction method in the initial VD microstructure. With this as the starting point, Forward Euler was implemented for the temporal evolution of junction positions. VD parameters, including the minimum inter-junction distance for T1 transformation and minimum grain area for T2 are listed in table 3.3.

Table 3.3: VD model parameters.

| **Dimensionless Parameter** | **Value** |
|---|---|
| System Size | 512 x 512 (From PFM) |
| dt | 1 |
| Total time, t | 3000 |
| $\gamma_m$ | 0.952 (From PFM) |
| Minimum node distance | 3 |
| Minimum Grain Area | 30 |
| Order parameter mobility, L | 1 (From PFM) |
| TJ mobility | 0.05 × L |
| $\theta_{\max}$ | 15° |

All the VD codes are developed using MATLAB. In the next chapter, the results of all the above models and simulations are discussed in detail.

# CHAPTER 4

# Results

## 4.1 Initial PFM microstructure

All the parameters in our PFM and VD simulations are dimensionless (termed as "simulation units" from now). Fig. 4.1 shows the 512 × 512 mesh grid of the initial microstructures in isotropic and anisotropic grain growth phase-field models. The starting point is essentially the same in both the cases and represents a liquid. The colorbar represents order parameters ranging from [0, 1] and each order parameter has orientation $\theta$ between 0° and 30°. The boundary function used to visualize the microstructures was $\sum_{i=1}^{n} \eta_i^2$, where n is the number of order parameters.

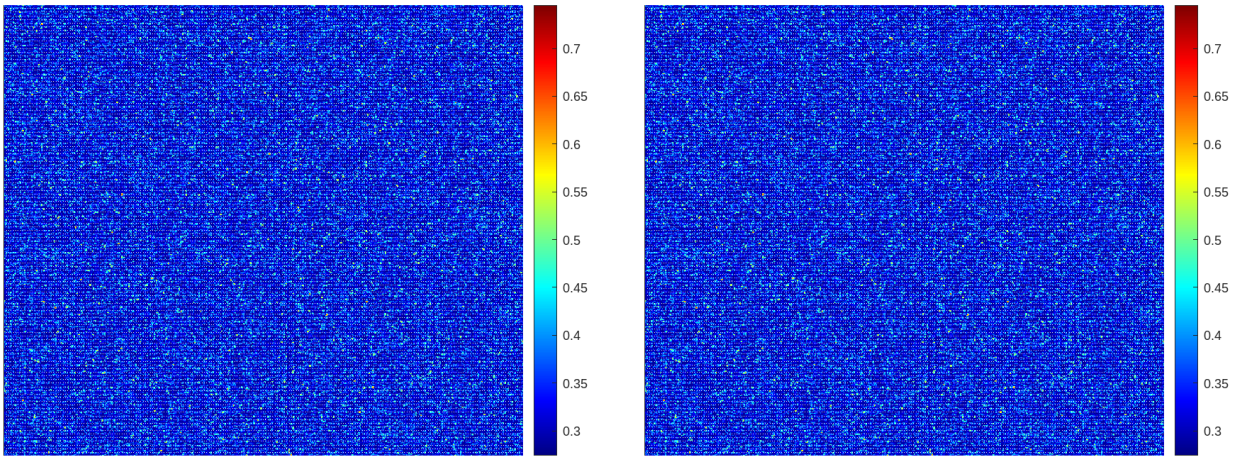


(a) (b)

Fig. 4.1: Initial microstructures in (a) isotropic and (b) anisotropic grain growth phase-field models.

## 4.2 Microstructure at t = 100

The evolved grain structures are illustrated in Fig. 4.2.

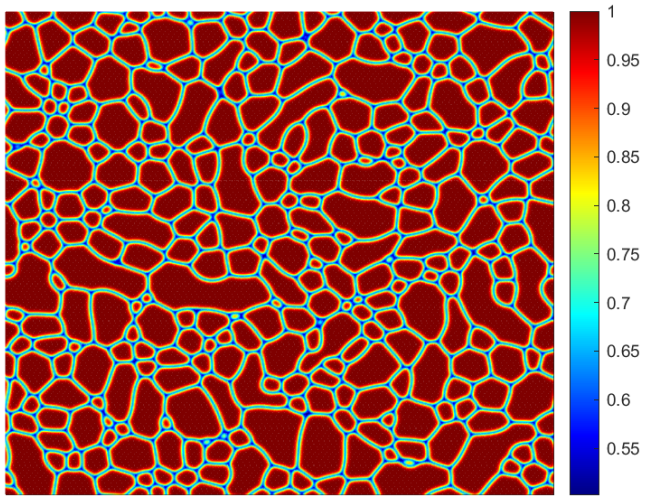


(a)

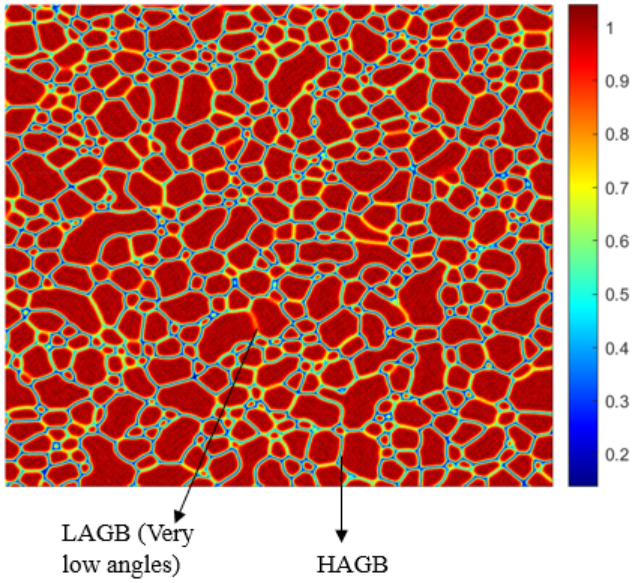


(b)

Fig. 4.2: Microstructures at t = 100 in (a) isotropic and (b) anisotropic grain growth.

A significant difference can be seen between Fig. 4.2(a) and 4.2(b) due to the anisotropic grain boundary energy. In the isotropic case, all the grain boundaries have the same energy. Also, for an astute observer, the grains appear to be larger and their distribution more

uniform when compared to anisotropic grain growth. On the other hand, in Fig. 4.2(b), the lighter (almost transparent) boundaries manifest very low-angle grain boundaries, and the gradual increase in darkness indicates a shift towards the high-angle grain boundary regime. Fig. 4.3 shows the misorientation distribution and the corresponding grain boundary energy dependence.

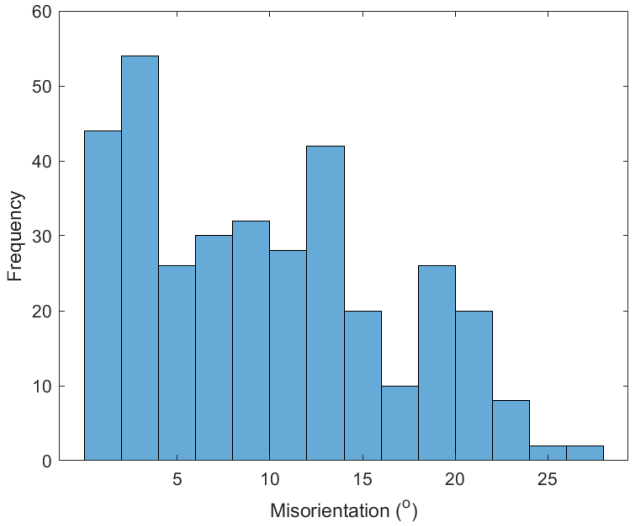


(a)

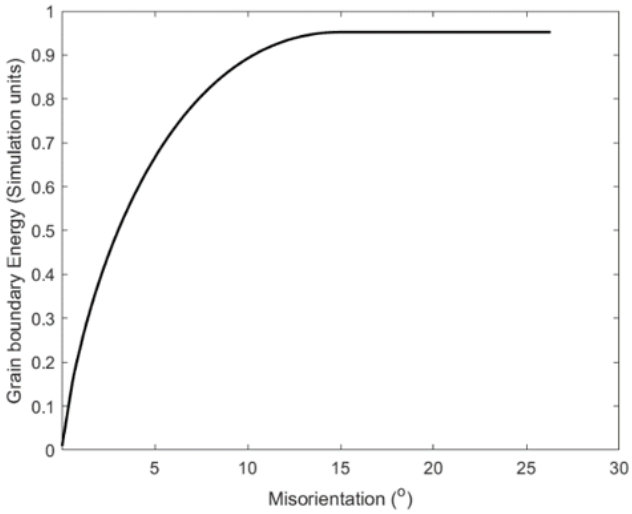


(b)

Fig. 4.3: (a) Misorientation distribution and (b) Variation of grain boundary energy with misorientation.

## 4.3 Identifying different grains from PFM and labeling them

An example of labeling the grains from PFM image is presented in Fig. 4.4 for the anisotropic microstructure. Each color represents a set of grains that belong to a same order parameter with a particular orientation. The conversion from 4.4(a) to 4.4(b) is essential to accurately distinguish the grain pixels from grain boundary pixels during the subsequent binary image conversion.

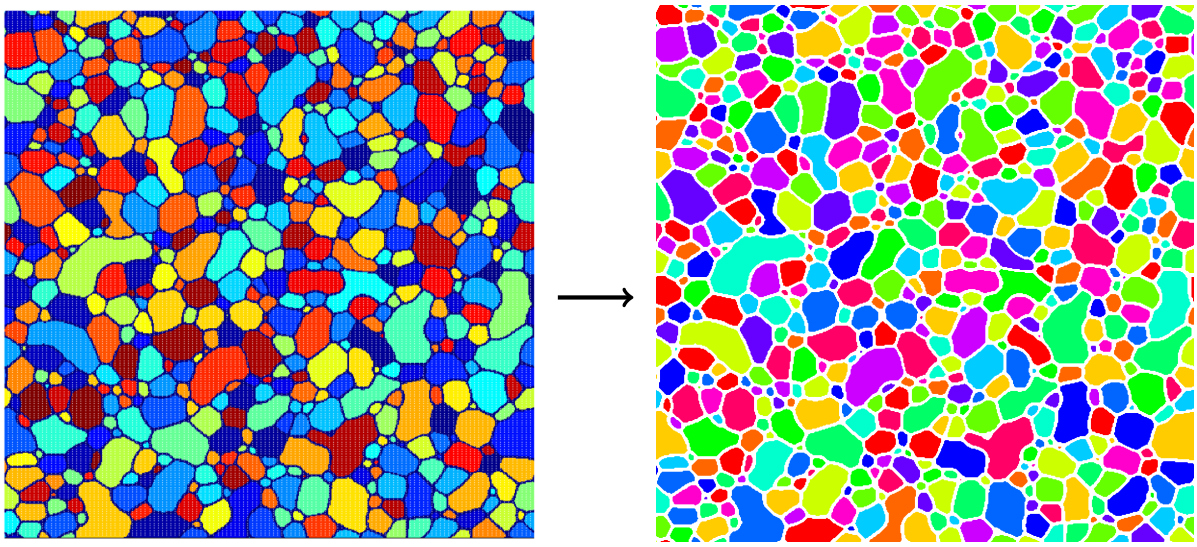

(a) (b)

Fig. 4.4: Anisotropic microstructure with (a) labeled grains (b) clear pixel distinction between grains and grain boundaries.

## 4.4 Implementation of Backpropagation Neural Network

Fig. 4.5 shows the final binary representation of the PFM microstructures given by NN. This process is developed such that the conversion is independent of the grain boundary thickness. To compare the features of the binary image obtained by the process we employed, with MATLAB's inherent Otsu's algorithm, the subtle differences in the identification of smaller

grains by the two methods are depicted in Fig. 4.6. In Fig. 4.6(a) and 4.6(c), there is some noise from the grain boundary pixels that interferes with accurate shape detection of the grain, while Fig. 4.6(b) and 4.6(d) capture a better overall shape.

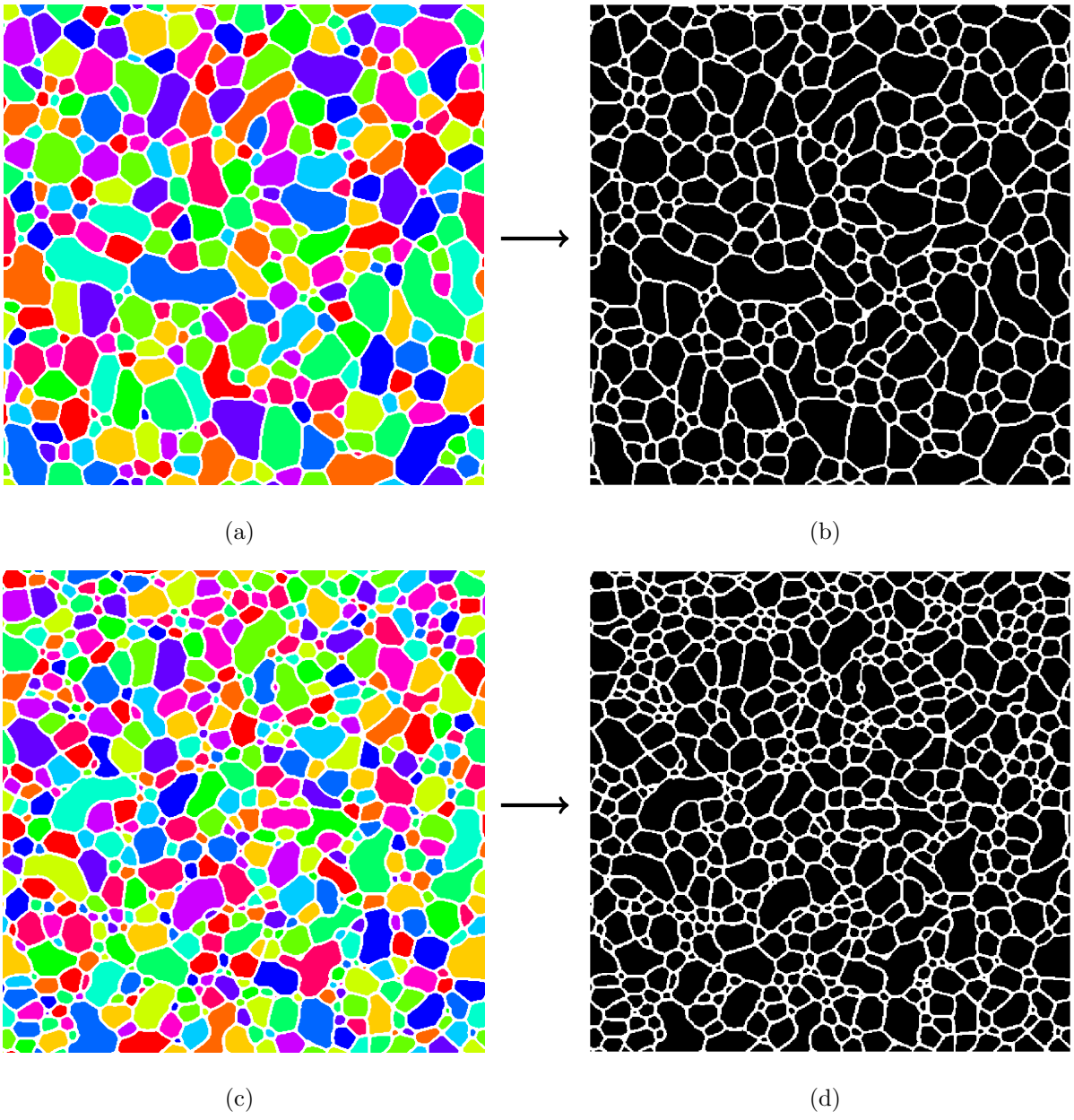

(a) (b)

(c) (d)

Fig. 4.5: Binary conversion of (a) isotropic and (b) anisotropic microstructure using Backpropagation neural network.

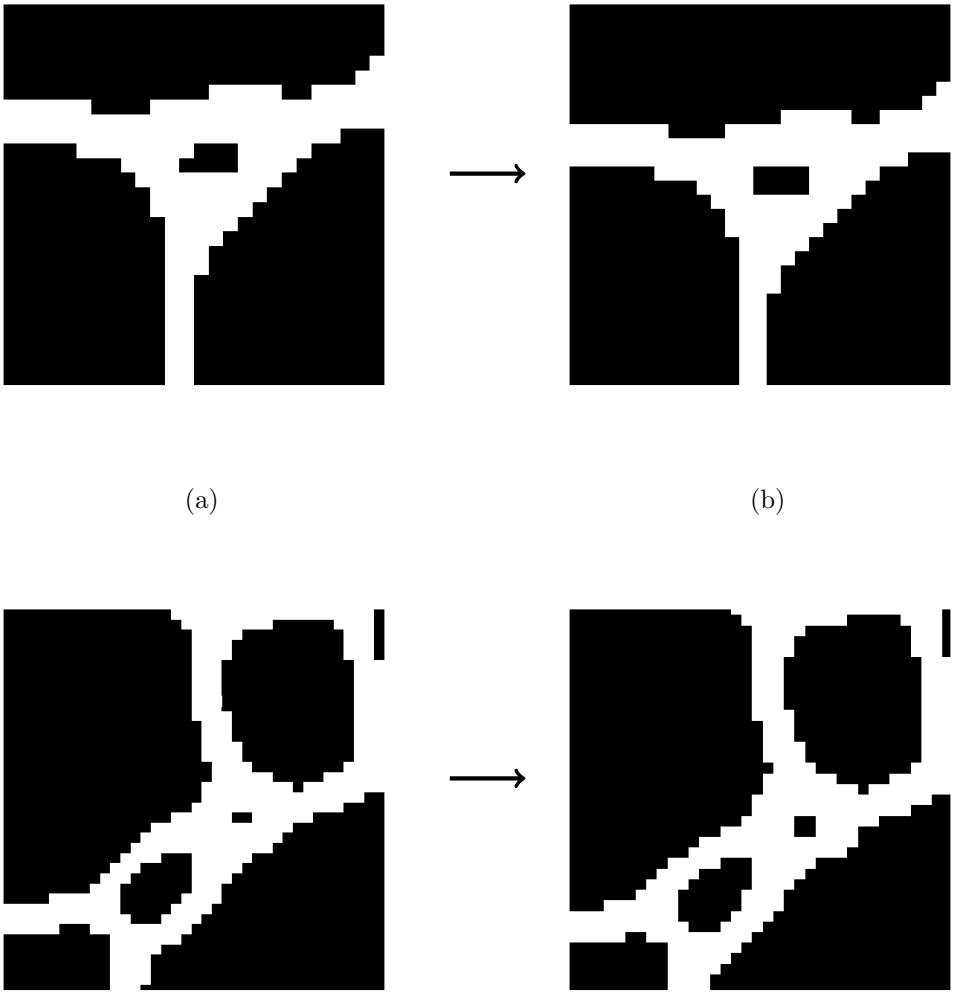

(a) (b)

(c) (d)

Fig. 4.6: A small grain detected by Otsu's method and denoised by Neural Network in (a), (b) isotropic and (c), (d) anisotropic microstructures.

## 4.5 Thinning of binary image

GBs with finite thickness from the binary microstructure are transformed by Zhang-Suen thinning algorithm into thin segments made up of single pixels. The results are displayed in Fig. 4.7.

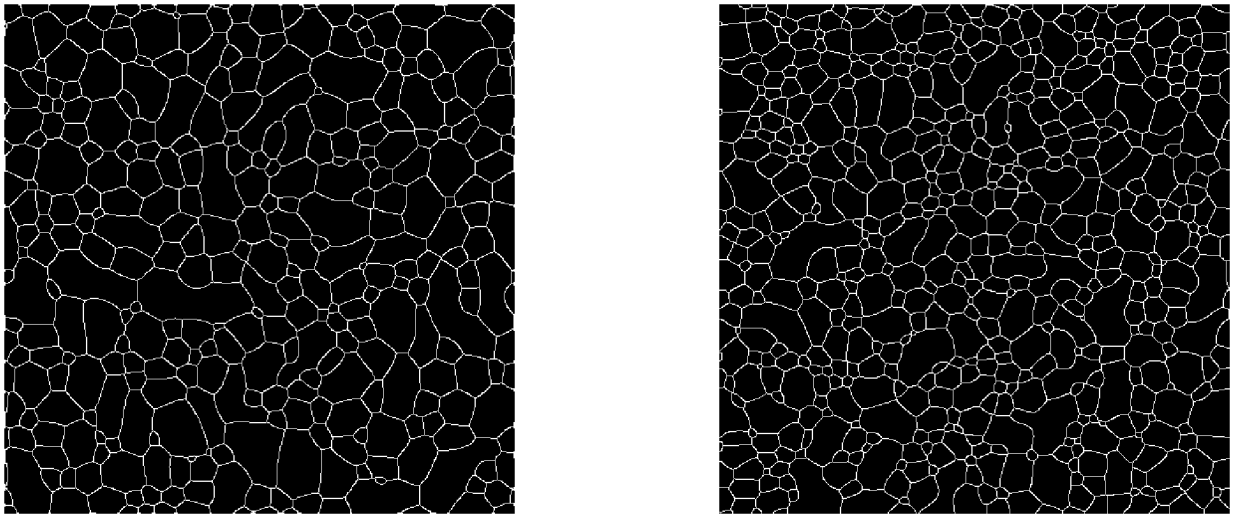

(a) (b)

Fig. 4.7: Thinned grain boundaries of (a) isotropic and (b) anisotropic microstructures with modified Zhang-Suen thinning algorithm.

## 4.6 Reassigning labels and finding grain, junction connectivity

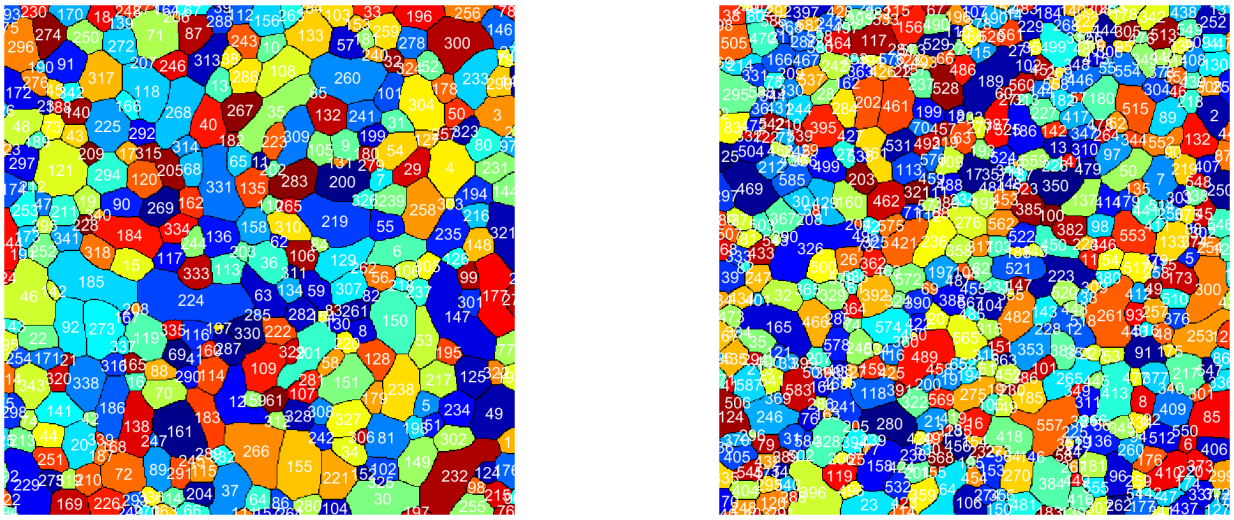

(a) (b)

Fig. 4.8: Relabeling of grains after thinning in (a) isotropic and (b) anisotropic microstructures.

The grain labels from PFM play an important role in our study. Based on the labels associated with individual grid points from Fig. 4.4 and pixel neighborhood from Fig. 4.7, the grains were identified with respect to pixel coordinates and relabeled. The results are shown in Fig. 4.8. The colors here do not represent different orientations, but are random. Further, the grains along the edges do not have identical labels although they are parts of the same grain due to periodicity. This, however, does not affect the evolution during VD.

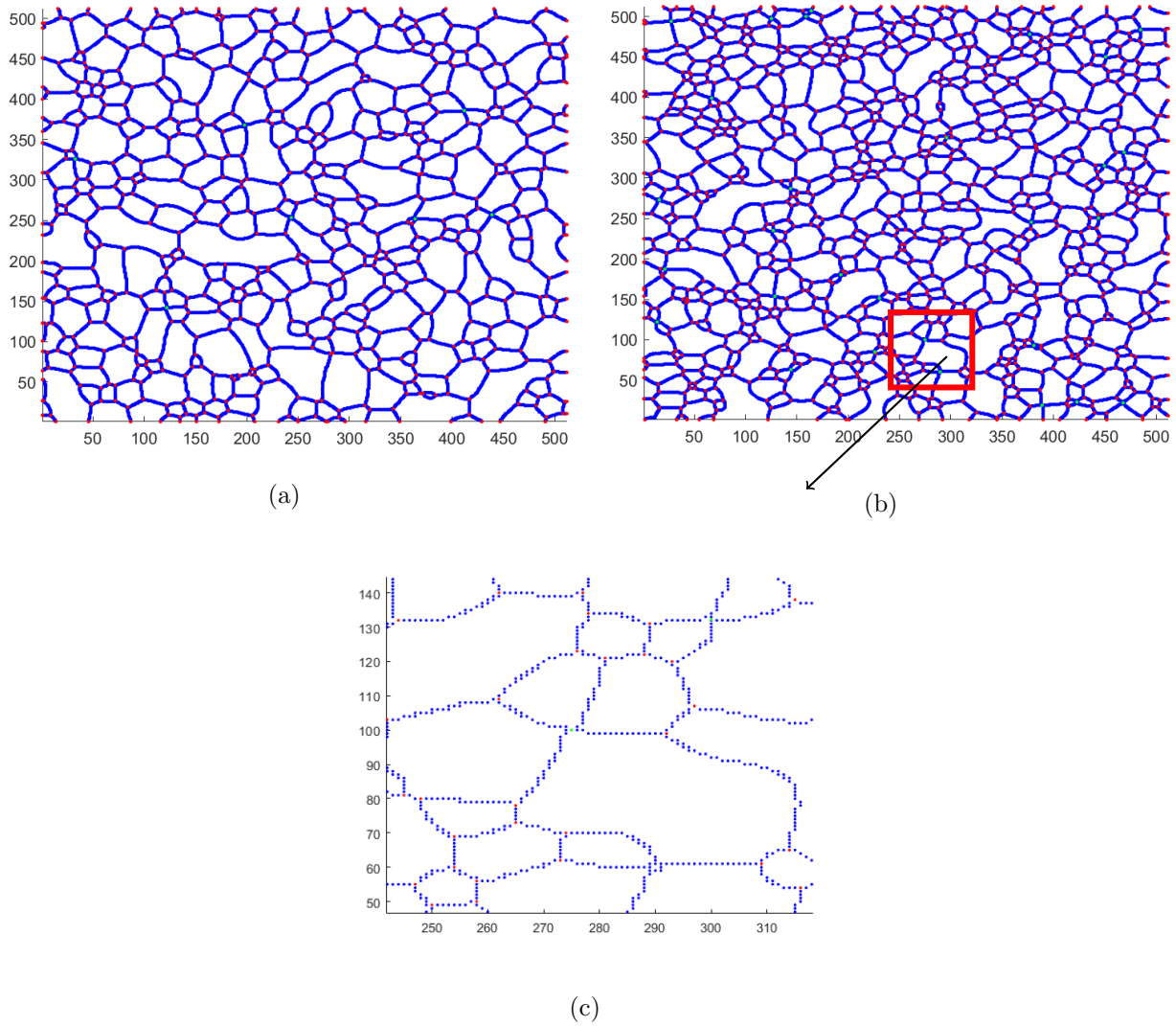


Fig. 4.9: (a) Isotropic and (b) Anisotropic microstructures represented by pixel coordinates. The red pixels indicate TJs and edge nodes. The green pixels represent QJs. (c) Magnified section of (b) displaying multiple TJs and QJs.

The microstructure in Fig. 4.9 is characterized by TJs, QJs and virtual vertices (blue), and is produced from scattering the pixel coordinates of all the grains from Fig. 4.8. This is a key step in our method, as it helps form the inter-grain, inter-junction, and grain-junction connections.

## 4.7 Vertex representation and comparison with PFM output

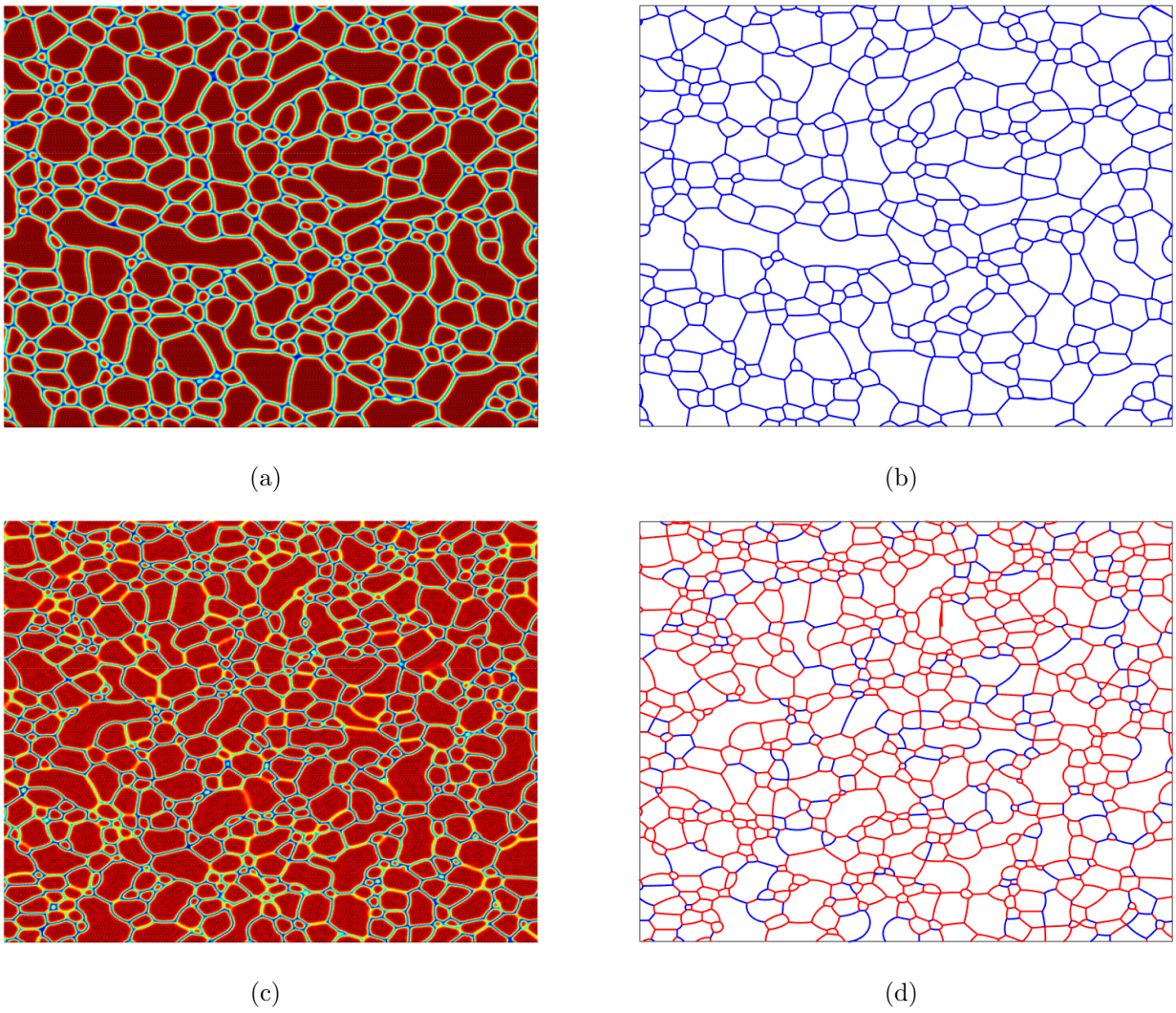

(a) (b)

(c) (d)

Fig. 4.10: Comparison of PFM output with VD input in (a), (b) isotropic and (c), (d) anisotropic microstructures. The red color in (d) represents LAGBs and blue, HAGBs.

Fitting circles along the virtual vertices between junctions and finding their radius leads to a vertex representation such as in Fig. 4.10 with finite GB curvatures, which is utilized as the initial condition for VD. One notable difference between the PFM and vertex structures is that smaller grains containing exactly "two" triple junctions are disappeared in the latter. This is analogous to T3 transformation in VD and does not significantly alter our outcome.

## 4.8 Microstructural evolution with VD

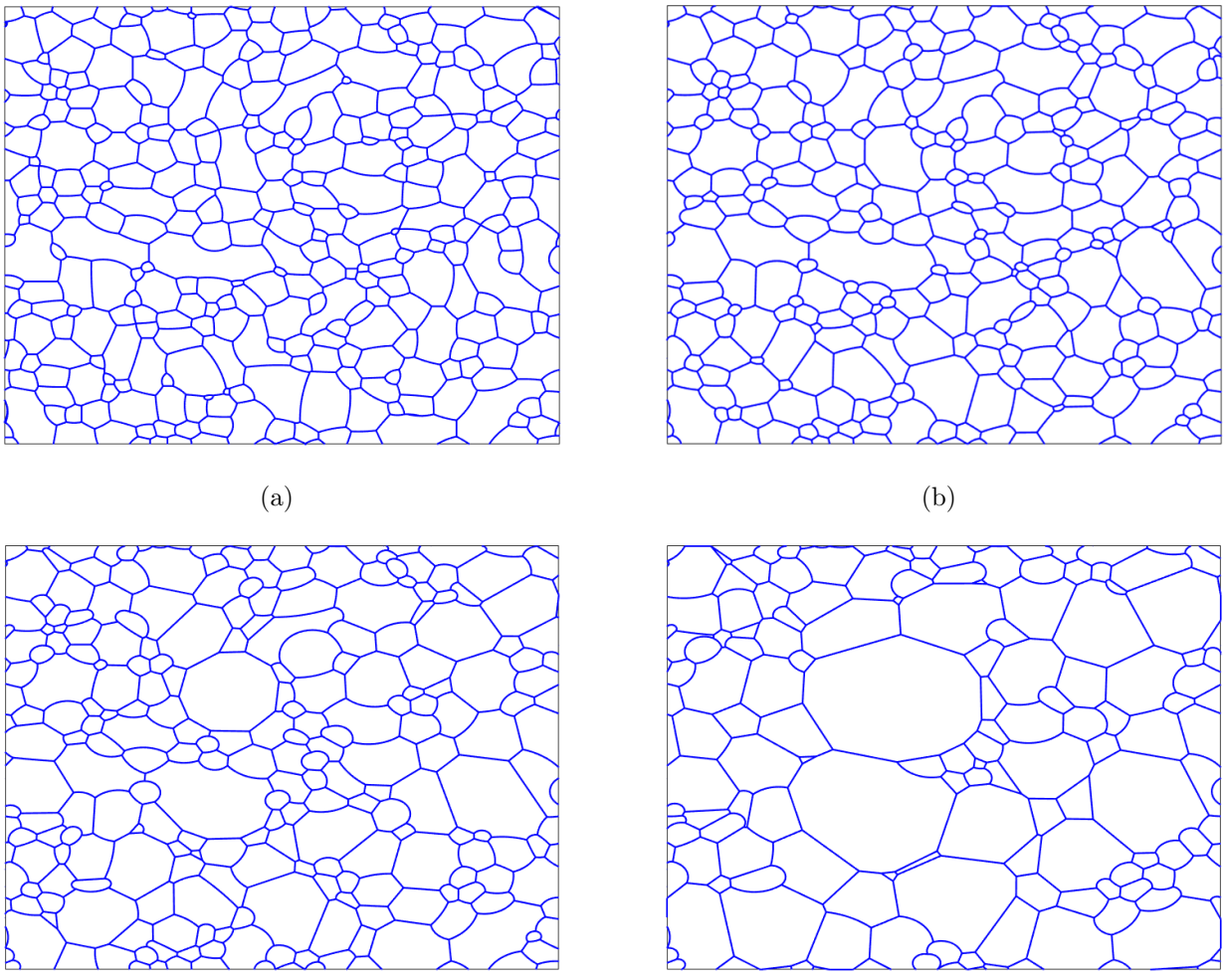

(a) (b) (c) (d)

Fig. 4.11: Isotropic grain growth in VD with input from PFM. Snapshots of microstructure at (a) t = 0, (b) t = 500, (c) t = 1500 and (d) t = 3000.

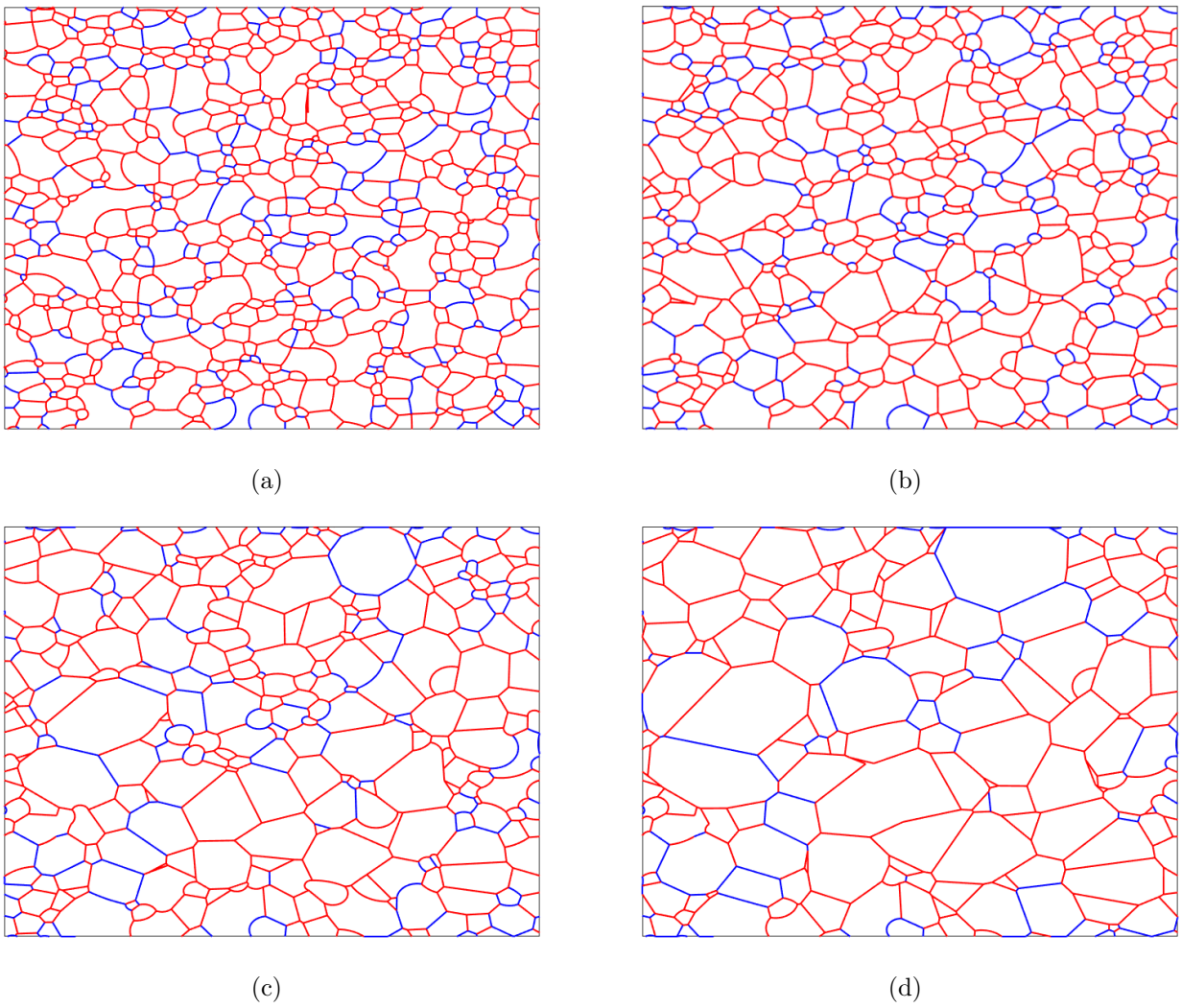


Fig. 4.12: Anisotropic grain growth in VD with input from PFM. Snapshots of microstructure at (a) t = 0, (b) t = 500, (c) t = 1500 and (d) t = 3000.

Fig. 4.11 and 4.12 show the grain evolution during VD. As indicated by the figures, the growth process is predominantly controlled by the low TJ mobility and the grains tend to achieve equilibrium dihedral angles, along with flattening of the GB curvatures. Further, in Fig. 4.12(d) the volume of high angle grain boundaries is greatly reduced, as expected from an anisotropic grain evolution.

Fig. 4.13(a) and 4.13(b) show the average grain size distribution in isotropic and anisotropic evolution. The self-similar nature can be observed in both the cases and the figures imply

that isotropic grain growth has a narrower distribution when compared to the anisotropic case. Also, the drastic decrease in number of grains in the anisotropic case can be attributed to the presence of unstable HAGBs.

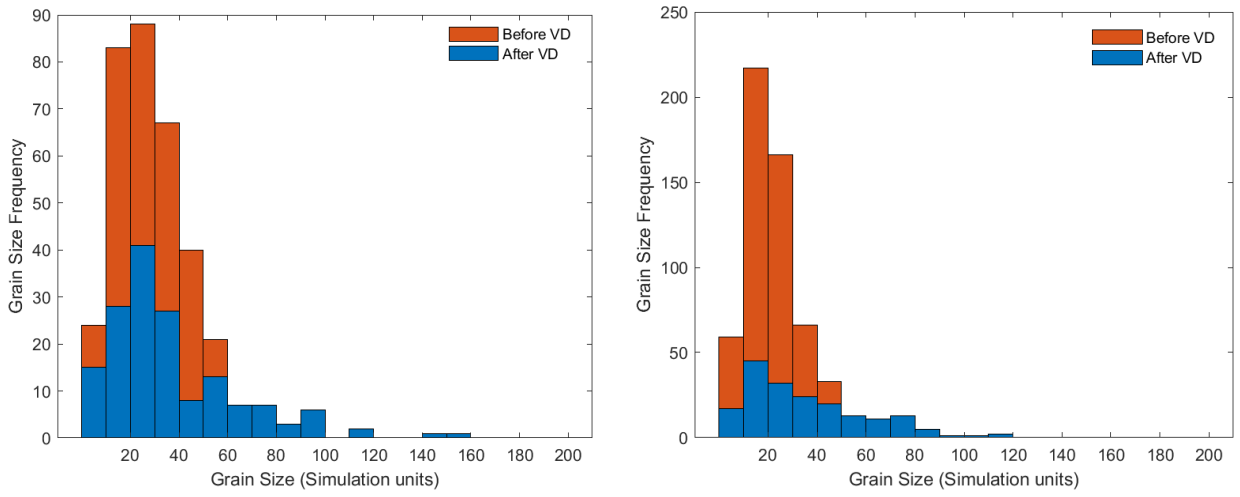


(a) (b)

Fig. 4.13: Grain Size Distribution before and after VD in (a) isotropic and (b) anisotropic grain growth.

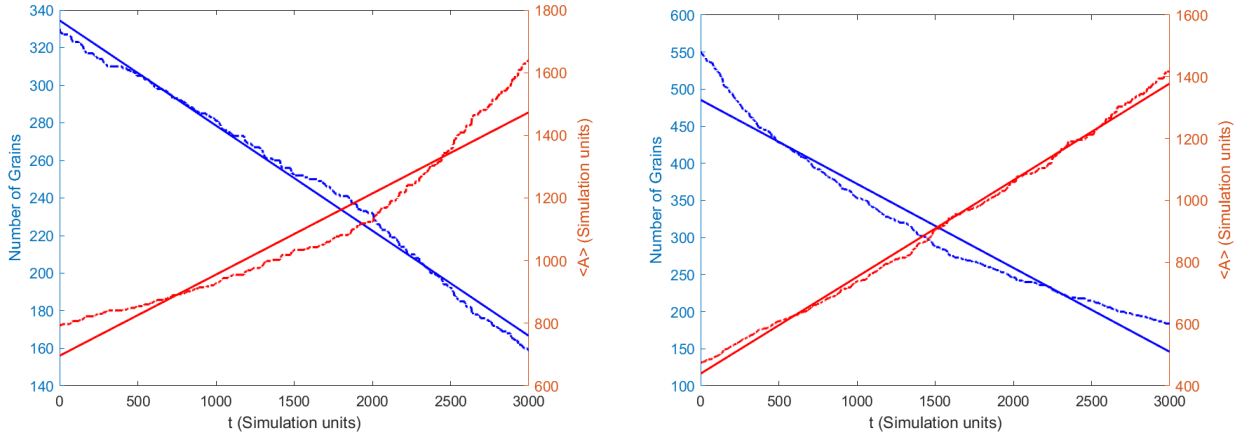


(a) (b)

Fig. 4.14: Variation of number of grains and average grain area with time in (a) isotropic and (b) anisotropic grain growth during VD simulation.

We also studied the variation in average grain area, $< A >$, and grain number with

time (refer to Fig. 4.14). The statistics are mostly consistent with the growth law kinetics. To further validate the model, we computed the dihedral angles at each junction. Fig. 4.15 displays the trend in dihedral angles from the final stage of PFM to the end of VD simulation. As growth progresses in isotropic microstructure, the angles approach the Herring equilibrium values of 120° and form a Gaussian-like distribution with a sharp peak. On the contrary, when GB energy anisotropy is present, the distribution gets broader due to a non-uniform propensity for migration in different GBs, although the system tries to lower its energy with a reasonable frequency of angles tending towards 120°. This is evident from Fig. 4.15(d).

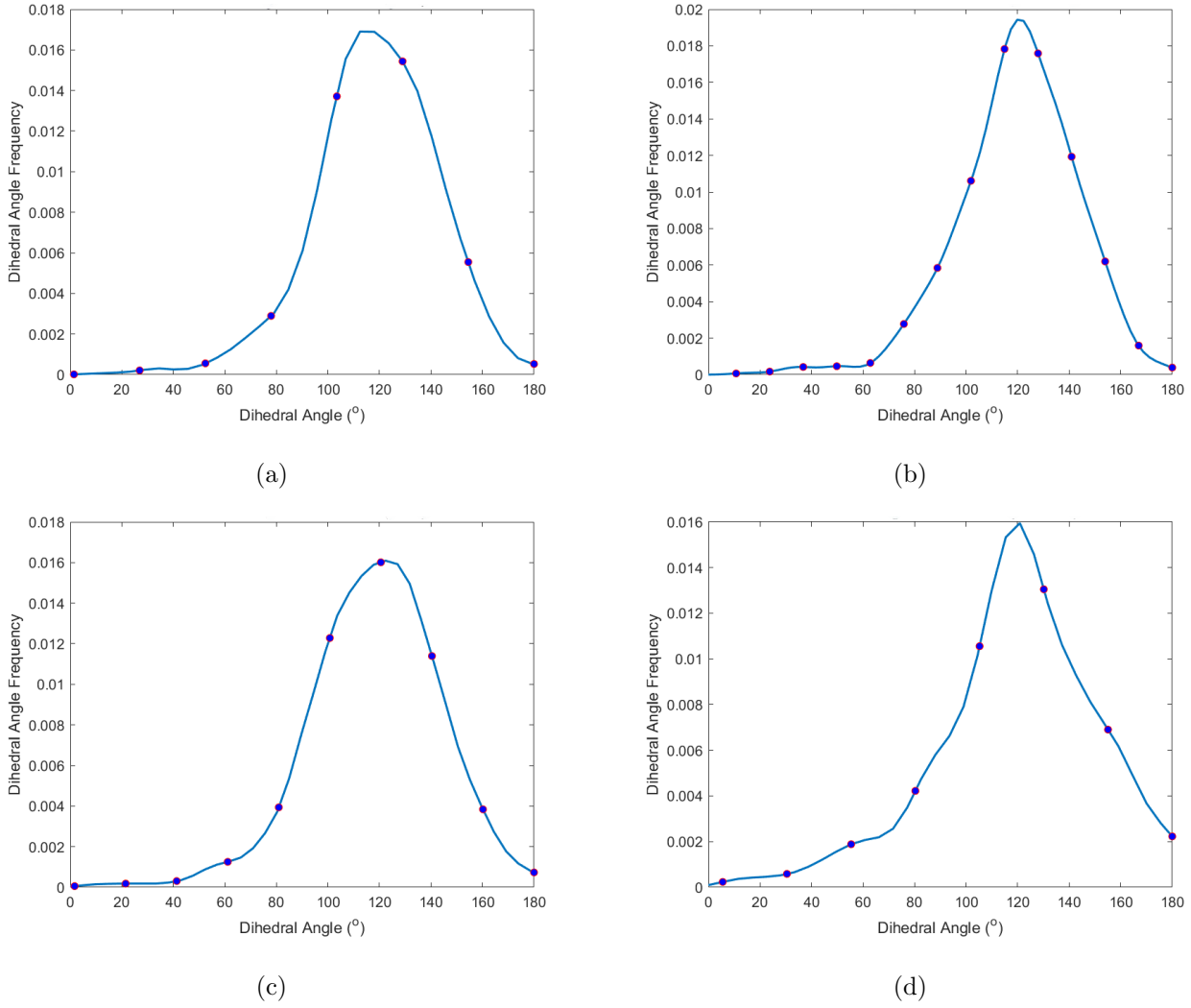


Fig. 4.15: Dihedral angle distribution in isotropic grain growth at (a) t = 0, (b) t = 3000, and in anisotropic grain growth at (c) t = 0, (d) t = 3000 during VD simulation.

# CHAPTER 5

# Discussion

Our results show that the microstructure from PFM can be efficiently transferred to the VD process. This has important implications with respect to the computational time and the accuracy of the VD model, in general. (1) Since various stages of grain growth have different dominant controlling mechanisms [77], incorporating every effect into a singular model may result in the increase of computational expenses, especially in cases where one of the mechanisms does not significantly impact the phenomenon. While the TJ effect has been incorporated into phase-field models previously [78, 79], our model offers greater flexibility and ease of handling the TJ motion due to VD. (2) The complexity in constructing the Voronoi tessellation is dramatically reduced, accompanied by a more realistic microstructural representation from PFM as the input to VD. The conversion of PFM output to a non-zero GB curvature vertex model takes only a few seconds with our method for any given microstructure generated by multi-order parameter phase-field model.

In addition, by knowing the relationship between order parameter mobility (and hence, GB mobility) and TJ mobility via the dimensionless parameter $\Lambda$, the transition from GB to TJ migration dominant regime during grain growth can now be efficiently modeled. This finite TJ mobility, often causing drag, is in turn contingent upon the distribution of dislocations or disconnections at the GBs, second phase particles and the back-stresses exerted by such morphological features. Finally, our model satisfies the well-established grain growth statistics, and has the potential to overcome the limitations of VD-like front tracking models mentioned in [80].

# CHAPTER 6

# Model Assumptions and considerations

The following assumptions and considerations are made in the development of our model.

1. The microstructure is described by a simple time-dependent Ginzburg-Landau free energy equation. The GB thickness is assumed to be constant.

2. Dimensionless parameters are used in all the simulations.

3. Misorientation between any two grains remains unaltered with time.

4. The effects of GB inclination, mobility anisotropy, dislocation motion and strain on grain growth are not taken into account. Although drag is introduced in the form of reduced TJ mobility ($\Lambda$), the reason for the same is not explicitly incorporated into our model. But it is possible to directly import these parameters from PFM simulation to VD using the same procedure employed in this study.

5. The GB and TJ mobilities are assumed to be temperature independent.

6. GB energy is calculated by a simplified Read-Shockley equation instead of the modified version or the energies determined by the experimental data of a material.

# CHAPTER 7

# Conclusion and future scope

The most important conclusions from our study are summarized below:

- We have developed a first-of-its-kind sequentially coupled phase-field and vertex dynamics model for grain growth in isotropic and anisotropic microstructures. One can switch from multi-order parameter phase-field to vertex dynamics model at any time depending on the material system and the prevalent mechanism during grain evolution.
- Every microstructure and parameter can be effectively transferred from PFM to VD model. Moreover, the grain boundary curvature is identified accurately using back-propagation neural network, image processing and local curvature calculations. This process is independent of the interface thickness in PFM.
- The VD model can now evolve complex microstructures from PFM, which is not possible with the conventionally used Voronoi tessellation, providing a more realistic approach to simulating grain growth with VD. The grain growth kinetics are also found to be in well agreement with the classical theories.
- The model, at its current state, is only a groundwork and a generalized model and its parameters can be modified based on material-specific needs. It leverages the advantages of both PFM and VD, and offers a new avenue for efficient isotropic and anisotropic grain growth simulations.

The future scope is to further extend the model to include mobility anisotropy, grain boundary inclination, defects and second phases, and possibly integrate it with the crystal plasticity-PFM based models to reduce the computational expenses.

# APPENDIX A

**Algorithm 3 :** Zhang-Suen Thinning Algorithm.

**Input:** Binary image `binaryImg`
**Output:** Thinned binary image `thinnedImg`
change ← true
**while** change **do**
  change ← false
  toRemove1 ← False matrix of size `binaryImg`
  toRemove2 ← False matrix of size `binaryImg`
  **for** $x, y \in \{2, \ldots, \text{rows} - 1\} \times \{2, \ldots, \text{cols} - 1\}$ **do**
    **if** `binaryImg`[x, y] $> 0$ **then**
      $P \leftarrow$ `binaryImg` neighbor pixels at $(x, y)$
      **if** $2 \leq \sum(P > 0) \leq 6$ **and** `transitions`$(P > 0) = 1$ **then**
        **if** $P[1] \cdot P[3] \cdot P[5] = 0$ **and** $P[3] \cdot P[5] \cdot P[7] = 0$ **then**
          toRemove1[x, y] ← true
          change ← true
        **end if**
      **end if**
    **end if**
  **end for**
  `binaryImg`[toRemove1] ← 0
  Repeat the loop with $P[1] \cdot P[3] \cdot P[7] = 0$ **and** $P[1] \cdot P[5] \cdot P[7] = 0$
  `binaryImg`[toRemove2] ← 0
**end while**
thinnedImg = binaryImg
**function** `transitions`(neighbors)
$\sum_{i=1}^{8}(neighbors[i] = 0$ **-** $neighbors[(i\%8) + 1] = 1)$
**end function**

# APPENDIX B

**Algorithm 4 :** Algorithm for establishing inter-junction, junction-grain and inter-grain connectivity based on pixel positions.

**Input:** Labeled $512 \times 512$ `grid`, number of grains `numGrains`

**Output:** `junctionPosition`, `junctionGrains`, `junctionConnect`, Grain boundary radius `GBRadius`, `junctionVelocity`

gridLength $\leftarrow$ length(grid)

**Extract grain and grain boundary (GB) pixel coordinates:**

(GBCoords, grainCoords) $\leftarrow$ Extract_Coordsgrid, numGrains

**Identify junctions and the grains they belong to:**

(junctionPosition) $\leftarrow$ Identify_Junctionsgrid, GBCoords, grainCoords

(junctionGrains) $\leftarrow$ junction_GrainsjunctionPosition, grainCoords, gridLength

**Determine junction connections:**

(junctionConnect) $\leftarrow$ Connected_JunctionsjunctionPosition, junctionGrains

**Initialize:** `junctionVelocity` $= 0$, `GBRadius` $= 0$

# Bibliography


[1] S.L. Semiatin, J.C. Soper, and I.M. Sukonnik. Short-time beta grain growth kinetics for a conventional titanium alloy. *Acta Materialia*, 44(5):1979–1986, 1996.

[2] Rohit Malik, Hyun-Min Kim, Young-Wook Kim, and Kwang Joo Kim. Grain-growth-induced high electrical conductivity in sic–bn composites. *Ceramics International*, 44(14):16394–16399, 2018.

[3] G.J. Fan, H. Choo, P.K. Liaw, and E.J. Lavernia. Plastic deformation and fracture of ultrafine-grained al–mg alloys with a bimodal grain size distribution. *Acta Materialia*, 54(7):1759–1766, 2006.

[4] A.V Sergueeva, V.V Stolyarov, R.Z Valiev, and A.K Mukherjee. Advanced mechanical properties of pure titanium with ultrafine grained structure. *Scripta Materialia*, 45(7):747–752, 2001.

[5] Jijun Ma, Xuyue Yang, Qinghuan Huo, Huan Sun, Jia Qin, and Jun Wang. Mechanical properties and grain growth kinetics in magnesium alloy after accumulative compression bonding. *Materials  Design*, 47:505–509, 2013.

[6] J.E. Burke and D. Turnbull. Recrystallization and grain growth. *Progress in Metal Physics*, 3:220–292, 1952.

[7] D G Cole, P Feltham, and E Gillam. On the mechanism of grain growth in metals, with special reference to steel. *Proceedings of the Physical Society. Section B*, 67(2):131, feb 1954.

[8] P. Feltham. Grain growth in metals. *Acta Metallurgica*, 5(2):97–105, 1957.

[9] M Hillert. On the theory of normal and abnormal grain growth. *Acta Metallurgica*, 13(3):227–238, 1965.

[10] I.M. Lifshitz and V.V. Slyozov. The kinetics of precipitation from supersaturated solid solutions. *Journal of Physics and Chemistry of Solids*, 19(1):35–50, 1961.

[11] G. Abbruzzese and K. Lücke. A theory of texture controlled grain growth—i. derivation and general discussion of the model. *Acta Metallurgica*, 34(5):905–914, 1986.

[12] N.P Louat. On the theory of normal grain growth. *Acta Metallurgica*, 22(6):721–724, 1974.

[13] H.V. Atkinson. Overview no. 65: Theories of normal grain growth in pure single phase systems. *Acta Metallurgica*, 36(3):469–491, 1988.

[14] Cyril Stanley Smith. Structure, substructure, and superstructure. *Rev. Mod. Phys.*, 36:524–532, Apr 1964.

[15] John Von Neumann. Metal interfaces. *American Society for Metals, Cleveland*, 108:108–110, 1952.

[16] W. W. Mullins. Two-Dimensional Motion of Idealized Grain Boundaries. *Journal of Applied Physics*, 27(8):900–904, 08 1956.

[17] N. Rivier. On the structure of random tissues or froths, and their evolution. *Philosophical Magazine B*, 47(5):L45–L49, 1983.

[18] S. K. Kurtz and F. M. A. Carpay. Microstructure and normal grain growth in metals and ceramics. Part I. Theory. *Journal of Applied Physics*, 51(11):5725–5744, 11 1980.

[19] Stewart K. Kurtz and F. M. A. Carpay. Microstructure and normal grain growth in metals and ceramics. part ii. experiment. *Journal of Applied Physics*, 51:5745–5754, 1980.

[20] Frederick John Humphreys and Max Hatherly. *Recrystallization and related annealing phenomena*. elsevier, 2012.

[21] P. Lin, G. Palumbo, J. Harase, and K.T. Aust. Coincidence site lattice (csl) grain boundaries and goss texture development in fe-3 *Acta Materialia*, 44(12):4677–4683, 1996.

[22] P.R. Rios. Abnormal grain growth development from uniform grain size distributions. *Acta Materialia*, 45(4):1785–1789, 1997.

[23] GS Grest, MP Anderson, DJ Srolovitz, and AD Rollett. Abnormal grain growth in three dimensions. *Scripta Metallurgica et Materialia*, 24(4):661–665, 1990.

[24] J. Dennis, Pete S. Bate, and John F. Humphreys. Abnormal grain growth in metals. In *Recrystallization and Grain Growth III*, volume 558 of *Materials Science Forum*, pages 717–722. Trans Tech Publications Ltd, 10 2007.

[25] Toshihiro Omori, Tomoe Kusama, Shingo Kawata, Ikuo Ohnuma, Yuji Sutou, Yoshikazu Araki, Kiyohito Ishida, and Ryosuke Kainuma. Abnormal grain growth induced by cyclic heat treatment. *Science*, 341(6153):1500–1502, 2013.

[26] Jianfeng Hu, Xianhao Wang, Junzhan Zhang, Jun Luo, Zhijun Zhang, and Zhijian Shen. A general mechanism of grain growth . theory. *Journal of Materiomics*, 7(5):1007–1013, 2021.

[27] U. Czubayko, V.G. Sursaeva, G. Gottstein, and L.S. Shvindlerman. Influence of triple junctions on grain boundary motion. *Acta Materialia*, 46(16):5863–5871, 1998.

[28] Suk-Joong L. KANG, Seok-Young KO, and Seung-Yoon MOON. Mixed control of boundary migration and the principle of microstructural evolution. *Journal of the Ceramic Society of Japan*, 124(4):259–267, 2016.

[29] D. Fan and L.-Q. Chen. Computer simulation of grain growth using a continuum field model. *Acta Materialia*, 45(2):611–622, 1997.

[30] Seong Gyoon Kim, Dong Ik Kim, Won Tae Kim, and Yong Bum Park. Computer simulations of two-dimensional and three-dimensional ideal grain growth. *Phys. Rev. E*, 74:061605, Dec 2006.

[31] Spencer L Thomas, Kongtao Chen, Jian Han, Prashant K Purohit, and David J Srolovitz. Reconciling grain growth and shear-coupled grain boundary migration. *Nature communications*, 8(1):1764, 2017.

[32] Shin Okita, Eisuke Miyoshi, Shinji Sakane, Tomohiro Takaki, Munekazu Ohno, and Yasushi Shibuta. Grain growth kinetics in submicrometer-scale molecular dynamics simulation. *Acta Materialia*, 153:108–116, 2018.

[33] Shin Okita, Eisuke Miyoshi, Shinji Sakane, Tomohiro Takaki, Munekazu Ohno, and Yasushi Shibuta. Grain growth kinetics in submicrometer-scale molecular dynamics simulation. *Acta Materialia*, 153:108–116, 2018.

[34] S. Raghavan and Satyam S. Sahay. Modeling the topological features during grain growth by cellular automaton. *Computational Materials Science*, 46(1):92–99, 2009.

[35] Y. Enomoto and R. Kato. Scaling behavior of two-dimensional vertex model for normal grain growth. *Acta Metallurgica et Materialia*, 38(5):765–769, 1990.

[36] Yoshiyuki Saito and Masato Enomoto. Monte carlo simulation of grain growth. *ISIJ International*, 32(3):267–274, 1992.

[37] Bimal K. Kad and Peter M. Hazzledine. Monte carlo simulations of grain growth and zener pinning. *Materials Science and Engineering: A*, 238(1):70–77, 1997.

[38] S A Wright, S J Plimpton, and T P Swiler. Potts-model grain growth simulations: Parallel algorithms and applications. 8 1997.

[39] Theron M. Rodgers, Jonathan D. Madison, and Veena Tikare. Simulation of metal additive manufacturing microstructures using kinetic monte carlo. *Computational Materials Science*, 135:78–89, 2017.

[40] Haijie Xu, Xuedao Shu, Jinrong Zuo, Anmin Yin, and Ying Wang. Kinetic monte carlo simulation of abnormal grain growth in textured systems with anisotropic grain boundary energy and mobility. *Materials Today Communications*, 30:103133, 2022.

[41] A. Kazaryan, Y. Wang, S. A. Dregia, and Bruce R. Patton. Generalized phase-field model for computer simulation of grain growth in anisotropic systems. *Phys. Rev. B*, 61:14275–14278, Jun 2000.

[42] C.E. Krill III and L.-Q. Chen. Computer simulation of 3-d grain growth using a phase-field model. *Acta Materialia*, 50(12):3059–3075, 2002.

[43] Hyun-Kyu Kim, Seong Gyoon Kim, Weiping Dong, Ingo Steinbach, and Byeong-Joo Lee. Phase-field modeling for 3d grain growth based on a grain boundary energy database. *Modelling and Simulation in Materials Science and Engineering*, 22(3):034004, apr 2014.

[44] Tatsuzo Nagai Kyozi Kawasaki and Katsuya Nakashima. Vertex models for two-dimensional grain growth. *Philosophical Magazine B*, 60(3):399–421, 1989.

[45] D. Weygand, Y. Bréchet, and J. Lépinoux. Zener pinning and grain growth: a two-dimensional vertex computer simulation. *Acta Materialia*, 47(3):961–970, 1999.

[46] L. Helfen, D.T. Wu, R. Birringer, and C.E. Krill. The impact of stochastic atomic jumps on the kinetics of curvature-driven grain growth. *Acta Materialia*, 51(10):2743–2754, 2003.

[47] Y.-W. Mai H. W. Zhang Y. G. Zheng, C. Lu and Z. Chen. Grain growth as a stochastic and curvature-driven process. *Philosophical Magazine Letters*, 86(12):787–794, 2006.

[48] Eric R. Homer, Veena Tikare, and Elizabeth A. Holm. Hybrid potts-phase field model for coupled microstructural–compositional evolution. *Computational Materials Science*, 69:414–423, 2013.

[49] Q.nbsp;Y. Xu and B.nbsp;C. Liu. Modeling of as-cast microstructure of al alloy with a modified cellular automaton method. *Materials Transactions*, 42(11):2316–2321, 2001.

[50] Anh Tran, Yan Wang, and Theron Rodgers. Data assimilation for microstructure evolution in kinetic monte carlo. In *TMS 2023 152nd Annual Meeting & Exhibition Supplemental Proceedings*, pages 561–575, Cham, 2023. Springer Nature Switzerland.

[51] Daniel Weygand, Y. Bréchet, and Joël Lépinoux. A vertex dynamics simulation of grain growth in two dimensions. *Philosophical Magazine Part B*, 78:329–352, 1998.

[52] Joël Lépinoux, Daniel Weygand, and Marc Verdier. Modeling grain growth and related phenomena with vertex dynamics. *Comptes Rendus Physique*, 11(3):265–273, 2010. Computational metallurgy and scale transitions.

[53] L. Mao H. S. Udaykumar and R. Mittal. A finite-volume sharp interface scheme for dendritic growth simulations: Comparison with microscopic solvability theory. *Numerical Heat Transfer, Part B: Fundamentals*, 42(5):389–409, 2002.

[54] C. Ming Huang, C.L. Joanne, B.S.V. Patnaik, and R Jayaganthan. Monte carlo simulation of grain growth in polycrystalline materials. *Applied Surface Science*, 252(11):3997–4002, 2006. ICMAT 2005: Symposium L.

[55] Saransh Choudhury and R. Jayaganthan. Monte carlo simulation of grain growth in 2d and 3d bicrystals with mobile and immobile impurities. *Materials Chemistry and Physics*, 109(2):325–333, 2008.

[56] Long-Qing Chen. Phase-field models for microstructure evolution. *Annual Review of Materials Research*, 32(Volume 32, 2002):113–140, 2002.

[57] John W. Cahn and John E. Hilliard. Free Energy of a Nonuniform System. I. Interfacial Free Energy. *The Journal of Chemical Physics*, 28(2):258–267, 02 1958.

[58] Johson William Cahn and Samuel Miller Allen. A microscopic theory for domain wall motion and its experimental verification in fe-al alloy domain growth kinetics. *Le Journal de Physique Colloques*, 38(C7):C7–51, 1977.

[59] Long-Qing Chen. Phase-field models for microstructure evolution. *Annual Review of Materials Research*, 32(Volume 32, 2002):113–140, 2002.

[60] Tatsuzo Nagai Kyozi Kawasaki and Katsuya Nakashima. Vertex models for two-dimensional grain growth. *Philosophical Magazine B*, 60(3):399–421, 1989.

[61] Takuo Kusaba Kazuhiro Fuchizaki and Kyozi Kawasaki. Computer modelling of three-dimensional cellular pattern growth. *Philosophical Magazine B*, 71(3):333–357, 1995.

[62] Joël Lépinoux, Daniel Weygand, and Marc Verdier. Modeling grain growth and related phenomena with vertex dynamics. *Comptes Rendus Physique*, 11(3):265–273, 2010.

[63] G Gottstein, A.H King, and L.S Shvindlerman. The effect of triple-junction drag on grain growth. *Acta Materialia*, 48(2):397–403, 2000.

[64] L.A. Barrales Mora. 2d vertex modeling for the simulation of grain growth and related phenomena. *Mathematics and Computers in Simulation*, 80(7):1411–1427, 2010. Multiscale modeling of moving interfaces in materials.

[65] G Gottstein, Y Ma, and LS Shvindlerman. Triple junction motion and grain microstructure evolution. *Acta Materialia*, 53(5):1535–1544, 2005.

[66] Nele Moelans, Frank Wendler, and Britta Nestler. Comparative study of two phase-field models for grain growth. *Computational Materials Science*, 46(2):479–490, 2009.

[67] Simon Daubner, Paul W. Hoffrogge, Martin Minar, and Britta Nestler. Triple junction benchmark for multiphase-field and multi-order parameter models. *Computational Materials Science*, 219:111995, 2023.

[68] Daniel A. Cogswell and W. Craig Carter. Thermodynamic phase-field model for microstructure with multiple components and phases: The possibility of metastable phases. *Phys. Rev. E*, 83:061602, Jun 2011.

[69] N. Moelans, B. Blanpain, and P. Wollants. Quantitative analysis of grain boundary properties in a generalized phase field model for grain growth in anisotropic systems. *Phys. Rev. B*, 78:024113, Jul 2008.

[70] L.Q. Chen and Jie Shen. Applications of semi-implicit fourier-spectral method to phase field equations. *Computer Physics Communications*, 108(2):147–158, 1998.

[71] Nobuyuki Otsu. A threshold selection method from gray-level histograms. *IEEE Transactions on Systems, Man, and Cybernetics*, 9(1):62–66, 1979.

[72] Hamed Mehrara, Mohammad Zahedinejad, and Ali Parsayan. Novel edge detection using bp neural network based on threshold binarization. In *2009 Second International Conference on Computer and Electrical Engineering*, volume 2, pages 408–412, 2009.

[73] T. Y. Zhang and C. Y. Suen. A fast parallel algorithm for thinning digital patterns. *Commun. ACM*, 27(3):236–239, mar 1984.

[74] G. Taubin. Estimation of planar curves, surfaces, and nonplanar space curves defined by implicit equations with applications to edge and range image segmentation. *IEEE Transactions on Pattern Analysis and Machine Intelligence*, 13(11):1115–1138, 1991.

[75] Cameron McElfresh and Jaime Marian. Initial grain orientation controls static recrystallization outcomes in cold-worked iron: Insight from coupled crystal plasticity/vertex dynamics modeling. *Acta Materialia*, 245:118631, 2023.

[76] G. Gottstein, A.D. Rollett, and L.S. Shvindlerman. On the validity of the von neumann–mullins relation. *Scripta Materialia*, 51(6):611–616, 2004.

[77] Spencer L. Thomas, Chaozhen Wei, Jian Han, Yang Xiang, and David J. Srolovitz. Disconnection description of triple-junction motion. *Proceedings of the National Academy of Sciences*, 116(18):8756–8765, 2019.

[78] A.E. Johnson and P.W. Voorhees. A phase-field model for grain growth with trijunction drag. *Acta Materialia*, 67:134–144, 2014.

[79] Simon Daubner, Paul W. Hoffrogge, Martin Minar, and Britta Nestler. Triple junction benchmark for multiphase-field and multi-order parameter models. *Computational Materials Science*, 219:111995, 2023.

[80] ZhangXinwei, ChenJiun-Shyan, and OsherStanley. A multiple level set method for modeling grain boundary evolution of polycrystalline materials. *Interaction and multiscale mechanics*, 1(2):191–209, 06 2008.